

## RESEARCH ARTICLE

10.1002/2017JB014296

## Key Points:

- Integrated 3-D density modeling is used to obtain a consistent model of the uppermost 200 km of the lithosphere in northern Argentina
- The crystalline crust shows complex thickness variations of lighter upper crust (2,800 kg/m<sup>3</sup>) and denser lower crust (3,100 kg/m<sup>3</sup>)
- The 3-D density model provides a basis for future studies of thermal and rheological variations

## Supporting Information:

- Supporting Information S1
- Data Set S1

## Correspondence to:

C. Meeßen,  
christian.meessen@gfz-potsdam.de

## Citation:

Meeßen, C., Sippel, J., Scheck-Wenderoth, M., Heine, C., & Strecker, M. R. (2018). Crustal structure of the Andean foreland in northern Argentina: Results from data-integrative three-dimensional density modeling. *Journal of Geophysical Research: Solid Earth*, 123, 1875–1903. <https://doi.org/10.1002/2017JB014296>

Received 7 APR 2017

Accepted 15 JAN 2018

Accepted article online 19 JAN 2018

Published online 12 FEB 2018

## Crustal Structure of the Andean Foreland in Northern Argentina: Results From Data-Integrative Three-Dimensional Density Modeling

C. Meeßen<sup>1,2</sup> , J. Sippel<sup>1</sup> , M. Scheck-Wenderoth<sup>1,3</sup>, C. Heine<sup>4,5</sup>, and M. R. Strecker<sup>2</sup> 

<sup>1</sup>GFZ German Research Centre for Geosciences, Potsdam, Germany, <sup>2</sup>Institute of Earth and Environmental Science, Potsdam University, Potsdam, Germany, <sup>3</sup>Department of Geology, Geochemistry of Petroleum and Coal, RWTH Aachen University, Aachen, Germany, <sup>4</sup>New Ventures, Upstream International, Shell International Exploration and Production B.V., The Hague, Netherlands, <sup>5</sup>Institute of Geology, Mineralogy and Geophysics, Ruhr-Universität Bochum, Bochum, Germany

**Abstract** Previous thermomechanical modeling studies indicated that variations in the temperature and strength of the crystalline crust might be responsible for the juxtaposition of domains with thin-skinned and thick-skinned crustal deformation along strike the foreland of the central Andes. However, there is no evidence supporting this hypothesis from data-integrative models. We aim to derive the density structure of the lithosphere by means of integrated 3-D density modeling, in order to provide a new basis for discussions of compositional variations within the crust and for future thermal and rheological modeling studies. Therefore, we utilize available geological and geophysical data to obtain a structural and density model of the uppermost 200 km of the Earth. The derived model is consistent with the observed Bouguer gravity field. Our results indicate that the crystalline crust in northern Argentina can be represented by a lighter upper crust (2,800 kg/m<sup>3</sup>) and a denser lower crust (3,100 kg/m<sup>3</sup>). We find new evidence for high bulk crustal densities >3,000 kg/m<sup>3</sup> in the northern Pampia terrane. These could originate from subducted Puncoviscana wackes or pelites that ponded to the base of the crystalline crust in the late Proterozoic or indicate increasing bulk content of mafic material. The precise composition of the northern foreland crust, whether mafic or felsic, has significant implications for further thermomechanical models and the rheological behavior of the lithosphere. A detailed sensitivity analysis of the input parameters indicates that the model results are robust with respect to the given uncertainties of the input data.

### 1. Introduction

The foreland of the central Andes is characterized by a change of deformation styles at about 23°S latitude (e.g., Jordan et al., 1983). North of this latitude, thin-skinned deformation dominates, where shortening is accommodated by décollements in thick Paleozoic to Tertiary sedimentary strata. In contrast, to the south, thick-skinned deformation with deep-seated reverse faults leads to spatially and temporally disparate uplift of basement-cored ranges. The mechanisms causing this change in deformation style have been a matter of discussion for more than two decades.

Early studies investigating the mechanisms causing this change pointed out the spatial coincidence of flat slab subduction (Jordan et al., 1983) and the absence of thick sedimentary strata (Allmendinger et al., 1983) in the thick-skinned provinces of the Andean foreland. Further mechanisms proposed are lithospheric thickening (e.g., Kley et al., 1999) and variations in the temperature and strength of the crystalline crust (e.g., Babeyko & Sobolev, 2005; Mon, 1979).

Although modeling by Babeyko and Sobolev (2005) confirmed the possibility of crustal strength variations as a cause for varying foreland deformation styles, there is little evidence for this hypothesis from integrated modeling. A data-integrative approach requires a model of the lithosphere and therefore profound knowledge of its composition and internal architecture. The structure and composition of the crust in particular are crucial parameters for the temperature distribution in the lithosphere and are therefore important factors influencing its rheological and geodynamic behavior (e.g., Burov et al., 1998; Scheck-Wenderoth et al., 2014).

Several studies have revealed the existence of different tectonic terranes constituting the crystalline crust beneath the Andean foreland basin; however, especially the boundary between the Río de la Plata craton and the Pampia terrane is still a matter of debate (e.g., Chernicoff & Zappettini, 2004; Peri et al., 2013, 2015; Ramos et al., 2010). Although some wells reach basement rocks (e.g., Marengo, 2015), the intracrustal structure and composition remain poorly constrained.

Well-mapped terrane boundaries also help provide an understanding of the nature of intraplate earthquakes, such as the 1811 earthquakes in New Madrid in the United States (Johnston & Schweig, 1996). With respect to the mainly east-west trending stress field in northern Argentina (e.g., Assumpcao, 1992), a north-south or northeast-southwest trending boundary between the Pampia terrane and Río de la Plata craton has significantly different implications on the seismic potential of the region. Given these problems, gravity-constrained density modeling is a method well suited for obtaining better insight into the compositional structure of the crystalline crust.

Density modeling utilizes the observed gravity field of the Earth to gain insight into its interior density structure. The deviations from the expected gravity field, the gravity anomalies, contain valuable information on the distribution of masses in the Earth's subsurface. However, direct inversion of observed gravity anomalies without additional data constraints does not yield a unique density distribution. To minimize this nonuniqueness of the density models, we integrated constraints on densities of major geological units and on the configuration of the first-order density interfaces within the lithosphere. First-order density interfaces generally exist between the atmosphere and the Earth's surface (topography), water bodies and the solid Earth (bathymetry), sediments and crystalline crust (basement), and at the crust-mantle boundary (Fowler, 1990).

Previously published gravity-constrained models of the central Andes and their foreland (Tassara, 2006; Tassara & Echaurren, 2012) have used approaches that filter the observed gravity field to obtain the geometries of these interfaces. However, although deep-seated density contrasts create long-wavelength anomalies in the observed gravity field, the argument that long-wavelength anomalies solely originate from deep-seated density contrasts is not straightforward. This is due to the fact that gravity anomalies are nonunique, and the superposition of density variations of different shapes can produce the same gravity anomaly if placed at different depths.

In light of these complexities, in this study we attempted to integrate observations that define the major density interfaces (between sediments, crystalline crust, and lithospheric mantle) a priori and derive the geometry of present-day intracrustal interfaces using three-dimensional density modeling. We assessed the validity of the inferred crustal density structure by performing a detailed sensitivity analysis of the model. The results of this study enable further evaluation of the thermal field and the rheological behavior of the lithosphere, so that primary mechanisms responsible for deformation style variations in the foreland of the central Andes can be identified.

### 1.1. Geological Setting

The South American continent is an amalgamation of Archean to Proterozoic terranes (Figure 1) that were accreted to its western margin in the Paleozoic (Almeida et al., 2000; Charrier et al., 2015; Ramos, 1988). During the formation of western Gondwana at around 620 Ma, the amalgamation of a series of terranes led to the 6,000 km long Transbrasiliano-Kandi mega shear zone (Cordani et al., 2013). In northern Argentina and Paraguay the Transbrasiliano Lineament (Figure 1), which is the southern manifestation of this shear zone, has been inferred to separate the Pampia terrane from the Río de la Plata craton (Cordani & Sato, 1999). The precise trajectory of this lineament in northern Argentina has been a matter of debate (Chernicoff & Zappettini, 2004; Ramos et al., 2010), but recently magnetotelluric studies (Peri et al., 2013, 2015) have favored the hypothesis posited by Ramos et al. (2010).

From the Ediacaran to the early Cambrian, the Puncoviscana formation, which consists of predominantly siliciclastic turbidites, deposited at the western margin of the Pampia terrane. The formation is found at present day in northern Argentina west of  $-64^{\circ}\text{E}$  within a 200 km wide band from the Bolivian border to Tucumán. The depositional setting of this formation has been a matter of debate, but geochemical analyses indicate that it originates from arc-like volcanic rocks, which has recently led Escayola et al. (2011) to propose a deposition west of a coeval arc terrane.

The amalgamation of continents was followed by a phase of extension during the early Paleozoic, when several basins formed along the Transbrasiliano Lineament, e.g., the Las Breñas half graben in northern

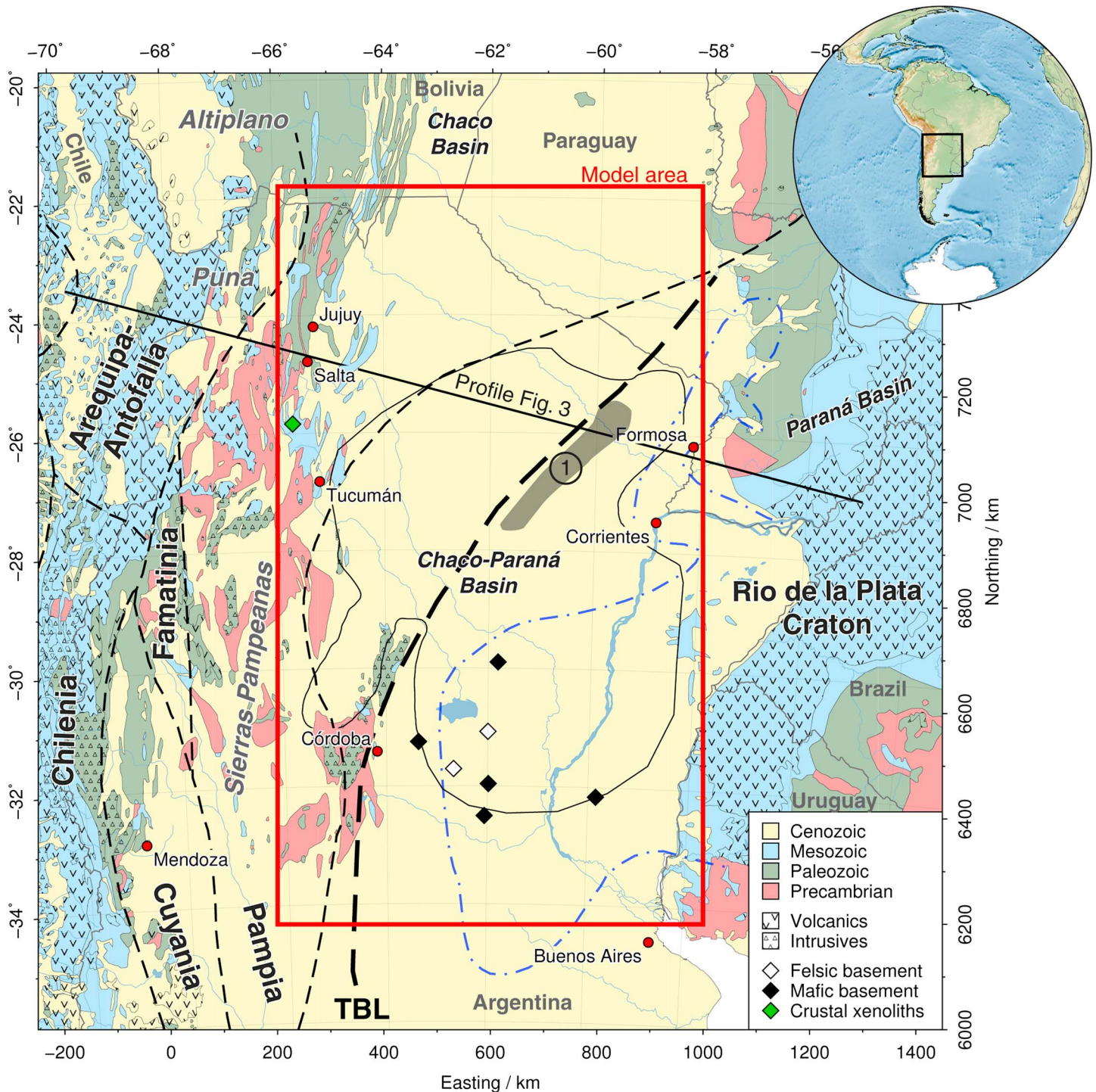


**Figure 1.** Map overview showing a simplified geology (Schenk et al., 2000), terranes, and the modeling area. The index map at the top right shows the map extent as a black rectangle. The density model area is outlined by the red box. Bold black dashed lines separate terranes and cratons that are in bold letters (Chernicoff & Zappettini, 2004). The thick dashed line marked TBL represents the Transbrasiliano Lineament (Peri et al., 2015; Ramos et al., 2010). The Las Breñas trough is marked by (1). The blue dash-dotted line marks the western extent of the Serra Geral flood basalts (Pezzi & Mozetic, 1989). Black/white diamonds indicate basement rock types observed in boreholes (Rapela et al., 2007; Winn & Steinmetz, 1998), green diamond is the sample location of lower crustal xenoliths (Lucassen et al., 1999).

Argentina (Figure 1 and Nr. 2 in Figure 2b). The Las Breñas formation that was deposited in the half graben consists of quartzites, siltstones, and claystones (Chebli et al., 1999) and, at present day, is situated at depths between 5 and 7.2 km. During the late Cambrian to the early Ordovician, thick sequences of gabbroanorites and diorites were emplaced into metasedimentary sequences at the western margin of the Famatinian terrane (Otamendi et al., 2009). Back-arc extension during Ordovician to Silurian times marked the first phase of areally extensive subsidence and sediment accumulation and initiated the Chaco-Paraná (CPB, Figure 1) and Paraná Basins (Milani & Zalan, 1999; Padula & Mingramm, 1963; Winn & Steinmetz, 1998). Both basins share a common evolution until the Late Cretaceous (Milani & Zalan, 1999). The present-day expression of the Neopaleozoic to Mesozoic depocenter of the CPB (Nr. 3 in Figure 2b) is a north-south elongated basin filled with up to 6 km of sediments.

At the beginning of the Silurian, during the Famatinian orogenic cycle, the northwestern Chaco plain was probably an integral part of a foreland basin (Mpodozis & Ramos, 1990; Winn & Steinmetz, 1998). The present-day manifestation of this paleo-foreland basin is a southwest to northeast trending basin up to 7 km deep that is limited to the west by the Andean orogenic wedge (1a and 1b in Figure 2b). The basin is mainly filled with quartzitic sandstones and micaceous shales (Chebli et al., 1999; Milani & Zalan, 1999). Deposits of the Gondwana I supersequence record the sedimentation history of the Paraná and Chaco-Paraná Basin from the late Carboniferous to the early Triassic (Milani & Zalan, 1999). The sequence comprises glacial sediments, conglomerates, sandstones to shales, and minor amounts of limestones and evaporites (Milani & Zalan, 1999). In the CPB, sediments equivalent to Gondwana I are dominated by siliciclastic deposits (Chebli et al., 1999; Milani & Zalan, 1999). Rifting and, ultimately, the opening of the South Atlantic during the Late Jurassic led to the formation of the conjugate margins of South America and southern Africa (e.g., Heine et al., 2013; Nürnberg & Müller, 1991). This episode was associated with the widespread extrusion of the Serra Geral flood basalts (Figure 1) in the Chaco-Paraná and Paraná Basins (Winn & Steinmetz, 1998). The basalts reach a thickness of up to 1.2 km in the east and gradually thin out westward (Chebli et al., 1999). Results from integrated density modeling indicate magmatic underplating in the Paraná Basin, inferred to have been associated with the eruption of the flood basalts (Dragone, 2013). Such underplating is not observed in the CPB, however, and may have contributed to the different evolution of the Chaco-Paraná and Paraná Basins in the Cenozoic.

The onset of the Andean uplift around 25 Ma (Mpodozis & Ramos, 1990) also marks the initiation of the Altiplano Plateau (Figure 1) and the present-day Chaco-Paraná foreland basin (Allmendinger et al., 1997; Isacks, 1988; Prezzi et al., 2014; Uba et al., 2006). Commencing uplift of the Puna Plateau bordering the Altiplano to the south was initiated between 20 and 15 Ma (Allmendinger et al., 1997). This early episode of the Andean orogeny was accompanied by the Laguna Pavia transgression from the late Oligocene to the early Miocene and was followed by the Entrerriense-Paranense transgression from the middle to late Miocene (Heine et al., 2015; Marengo, 2015; Ramos & Alonso, 1995). Both transgressions deposited sandstones, clay, and mudstone in the Chaco plain (Marengo, 2015). The Entrerriense-Paranense transgression reached as far inland as the region of the northwestern Sierras Pampeanas, which were uplifted after 13 Ma, marking the initiation of thick-skinned tectonics and the onset of the broken-foreland structural province (Bossi et al., 2001; Strecker et al., 1989). At the time, underthrusting of the Brazilian shield beneath the Andean orogen led to thickening of the lithosphere beneath the Altiplano plateau to 60–70 km (DeCelles & Horton, 2003). Between 12 and 6 Ma, shortening in the Altiplano ceased and shifted eastward into the foreland (Allmendinger et al., 1997). In contrast, shortening in the Puna plateau continued until 2–1 Ma (Allmendinger et al., 1989).

As a result of the tectono-sedimentary history, most of the crystalline basement in the CPB today is covered by sediments. Accordingly, little information is available from field studies on the configuration and composition of the crystalline basement.

Geophysical observations on the intracrustal structure were obtained during the PANDA and CHARGE seismic experiments, which explored the vertical velocity structure of the Cuyania, Pampia, and Famatinia terranes (Figure 1) (Alvarado et al., 2007). The authors inferred a rather felsic, quartz-rich composition for the Pampia terrane and the Río de la Plata craton from low  $v_p$  and  $v_p/v_s$  ratios. The authors' inferences on the composition of the Pampia terrane agree with basement outcrops of granites and migmatites in the Sierras Pampeanas (Mon, 1979; Simpson et al., 2003) but contrast with observations taken from drill cores of the southern Río de la Plata craton (diamonds in Figure 1). In addition to felsic basement rocks (granite and quartzite), mafic rocks (gabbro and granodiorite) were also identified as the plutonic crystalline basement in five out of seven wells that reached basement (Rapela et al., 2007; Winn & Steinmetz, 1998).

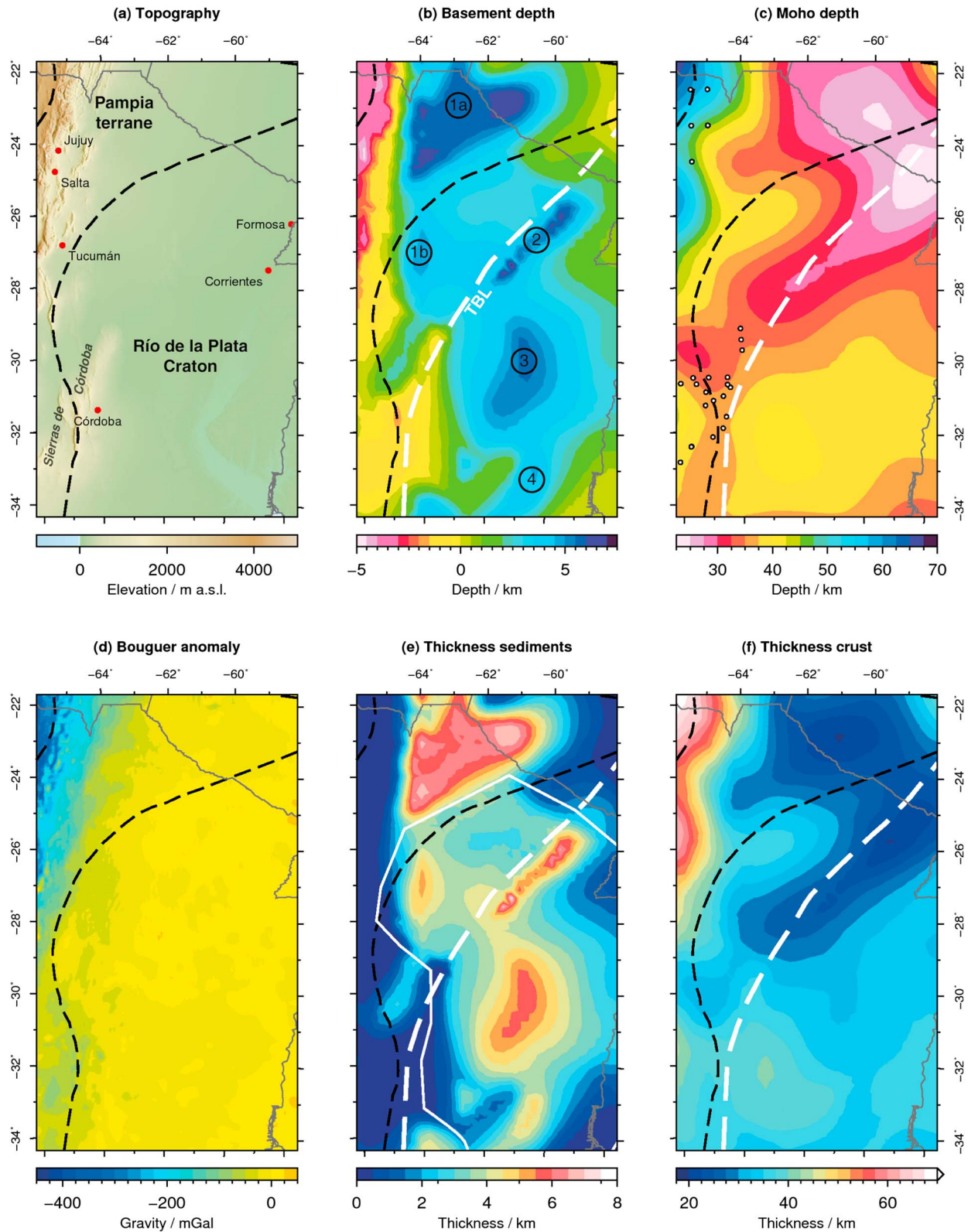


**Figure 2.** Initial model configuration: (a) topography (Amante & Eakins, 2009); (b) basement depth derived from sediment thickness map with main features: 1a)/1b) Silurian-Devonian foreland basin, 2) Las Breñas trough, 3) Neopaleozoic to Mesozoic depocenter, 4) Rosario subbasin (Pezzi & Mozetic, 1989; Ramos, 1999); (c) Moho depth from Model B2 (Assumpção et al., 2013) with point constraints indicated by circles; (d) free-air anomaly map (Barthelmes & Köhler, 2012; Förste et al., 2014); (e) sediment thickness derived from C. Heine (personal communication, 2016) and Pezzi and Mozetic (1989), the area to the SE of the white line is derived from the latter; (f) thickness of the crust derived from the top crystalline basement and the Moho depth.

A recent study exploited local seismic events in the southeastern Sierras Pampeanas to obtain high-frequency receiver functions (Perarnau et al., 2012). The authors found that the Moho lies around 35 km beneath the city of Córdoba and deepens to about 39 km at the western end of the Sierras de Córdoba (Figure 2a). They discovered two to three intracrustal interfaces, of which the deepest lies between 22 and 27 km depth, and an average  $v_p$  of 6.2 km/s for the crust.

Early tomographic studies in South America already identified an average depth of the Moho below the CPB of 32 km (Snoke & James, 1997). This was confirmed by Assumpção et al. (2013) and Rosa et al. (2016), who inferred Moho depths of up to 28 km below the CPB. Snoke and James (1997) identified a rather asthenospheric character for the upper mantle below the CPB with  $S$  wave velocities of about 4.2 km/s. Assumpção et al. (2013) obtained velocities between 4.3 and 4.2 km/s in the upper mantle below the northwestern part of the CPB, and higher shear wave velocities of 4.5 to 4.6 km/s in the south of the CPB (section 2.3.3). At greater depths, the velocity pattern inverts, and areas of former low velocity display high velocities. A high-velocity zone is furthermore observed above the flat slab beneath the Sierras Pampeanas, which coincides with a zone of increased seismicity and lower temperatures (Marot et al., 2014).

West of the modeled area, the Nazca Plate is being subducted beneath the South American continent. The subduction angle between 15 and 27°S latitude is about 30° and becomes subhorizontal between 27 and 32°S (Cahill & Isacks, 1992).

## 2. Methods and Data

We followed a stepwise approach of data integration and three-dimensional modeling, incorporating forward and inversion techniques. Therefore, we first defined the geometry for the starting structural and density model.

These geometries intend to represent the major density interfaces in the lithosphere and delineate the boundaries for bodies with similar physical properties. We approximated these bodies as units of homogeneous density and tested the impact of their geometrical configuration on the gravity field. The respective densities assigned to these bodies are in agreement with available geological observations.

We used the misfit between observed and predicted gravity fields to invert for variations in the interface of a lighter upper and a heavier lower crystalline crust. Throughout the inversion, only the interface between these two units was calculated. To further assess the validity of the obtained differentiated crystalline crust, we calculated the isostatic response of the model, assuming local isostasy. Finally, we performed a sensitivity analysis in which we also assessed the impact of mantle density variations.

### 2.1. Setup of Starting Structural and Density Model

During structural modeling, we defined the major density interfaces within the lithosphere: the topography, the top of the crystalline basement, and the Moho. The data for these interfaces were collected from literature and gridded onto regular two-dimensional grids using the convergent interpolation by Petrel (© Schlumberger Ltd.). The structural model covers the map area of Figure 1 with a lateral grid resolution of  $25 \times 25$  km and extends in depth from the topography down to 200 km.

#### 2.1.1. Data on Structural Interfaces

The topography (Figure 2a) was obtained from ETOPO1 (Amante & Eakins, 2009), which we used to infer the basement depth from sediment isopachs. For the CPB, we used isopach maps by Pezzi and Mozetic (1989). The remaining parts of the area were complemented by sediment thickness data from a global sediment thickness compilation of the Exxon Tectonic Map of the World (Exxon, 1985), which had been regridded using spherical splines in tension at a grid increment of 6 arc minutes. The compiled sediment thickness map and resulting basement depth are plotted in Figures 2e and 2b, respectively. To derive the depth to the top of the crystalline basement, the total sediment thickness was subtracted from the topography.

The Moho depth corresponds to model B2 of Assumpção et al. (2013), which mainly takes into account seismic point constraints (seismic reflection/refraction and receiver functions; dots in Figure 2c), waveform modeling, and Rayleigh wave group dispersion. Note that in the largest part of the model area, point constraints are absent. Additionally, the authors fitted oceanic areas by an empirical relationship between Bouguer anomaly and crustal thickness from the given seismic point constraints. Around the seismic point constraints, the error of Moho depth is estimated around  $\pm 4$  km (Assumpção et al., 2013).

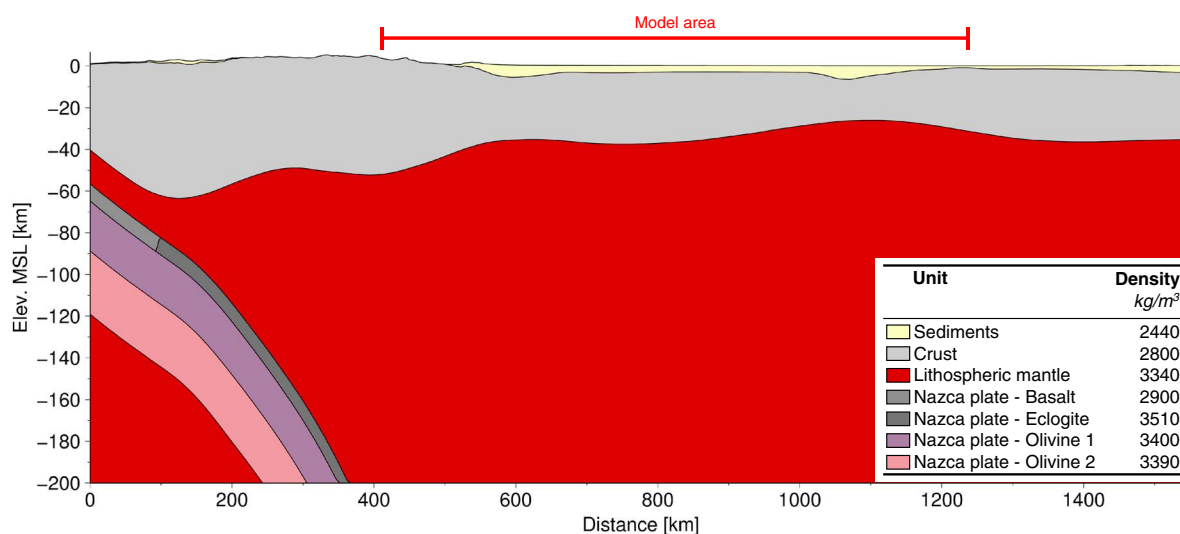


**Figure 3.** Initial model setup (vertical exaggeration: 3 times) with individual densities of the extended density model with homogeneous crust. For profile location, see Figure 1.

We implemented the subducting Nazca Plate using digitized depth contours from Tassara (2006). The bodies of the Nazca Plate were adapted from Kirchner (1997), who subdivided the plate into three bodies, of which the upper body is the oceanic crust composed of basalt, which transforms into eclogite at a depth of about 80 km (Figure 3). The lithospheric mantle is represented by a rigid upper body (Olivine 1) and a plastic transition layer (Olivine 2). The individual thickness relations of these bodies (8 km oceanic crust or 8 km eclogite, 23 km olivine layer 1, and 29 km olivine layer 2) were adapted from Kirchner (1997) as well. To account for the dip  $\alpha$  of the Nazca Plate, we calculated the true vertical thickness  $h$  according to  $h = t \cos^{-1} \alpha$ , where  $t$  is the thickness of the individual layer.

Although gravitational attraction decays  $\propto r^{-2}$ , strong density contrasts can impact the gravity field at great distance. Therefore, we extended the modeling area (red rectangle, Figure 1) to include the far-field influence of the subducting Pacific Plate beneath South America. For the impact of the modeled Nazca Plate on the gravity field of the modeling area, see Figure S15 in the supporting information.

## 2.2. Density Modeling

We differentiated bodies confined between the main density interfaces within the Earth. The stronger the contrast in density and the shallower the interface, the greater the impact of an individual body on the gravity field. At the same time, shallow density contrasts, for example, between crystalline crust and sediments, cause gravity anomalies of shorter wavelengths than deeper density contrasts, as, for example, in the crystalline crust or the upper mantle (e.g., Fowler, 1990).

### 2.2.1. Gravity Observations

For density modeling, we used the global EIGEN-6C4 model (Förste et al., 2014) up to degree 2190 with mean tide, obtained from the International Centre for Global Earth Models website (Barthelmes & Köhler, 2012). According to the functions implemented on the website, the gravity model was reduced to Bouguer anomaly using ETOPO1 (Amante & Eakins, 2009) with the same degree as the gravity model and a crustal density of  $\rho_c = 2,670 \text{ kg/m}^3$ . For elevations below mean sea level, that is, in the oceans, a density of  $\rho_w = (2,670 - 1,025) \text{ kg/m}^3$  was applied. The resulting Bouguer gravity field (Figure 2d) was then regridded onto a  $10 \times 10 \text{ km}$  regular grid, covering the area of interest (red square, Figure 1).

## 2.3. Density Constraints

### 2.3.1. Sediments

For the basin fill of the CPB, we assumed a homogeneously dense body composed of siliciclastic rocks (section 1.1). To determine a representative density for this body, we integrated Athy's law of compaction (Athy, 1930) over the maximum sediment thickness of 7.2 km (Figure 2e and Appendix A).

Applying  $\phi_0 = 0.41$  and  $k = 0.31 \text{ km}^{-1}$  for typical sandstone (Hantschel & Kauerauf, 2009) yields an average density of approximately  $2,440 \text{ kg/m}^3$  for the sediment body.

**Table 1**

*Mineral Assemblages Used for the Conversion From Shear Wave Velocity to Density in the Upper Lithospheric Mantle Between Depths of 50 and 200 km*

Name	OI (%)	Cpx/Di (%)	Opx/En (%)	Sp (%)	Gnt (%)	XFe	Source
Xenolith	75.4	4.6	18.7	1.3	0.0	8.6	Comin-Chiaramonti et al. (1986)
HP_Tc2	61.1	9.6	20.4	0.0	9.0	8.1	Griffin et al. (2009)
HP_Tc3	65.8	7.5	17.1	9.6	0.0	8.2	Griffin et al. (2009)
Off-cratonic	68.0	11.0	18.0	0.0	3.0	10.0	Shapiro and Ritzwoller (2004)

*Note.* We normalized the sum of the mineral phases to 100%. OI, olivine; cpx, clinopyroxene; di, diopside; opx, orthopyroxene; en, enstatite; sp, spinel; gnt, garnet; XFe, iron content.

### 2.3.2. Continental Crust and Nazca Plate

The density of the crystalline crust was prescribed as 2,800 kg/m<sup>3</sup>, which is consistent with estimates for the upper crust by made Kirchner (1997) and Lucassen et al. (2001) as well as estimates for metamorphic crustal rocks by Vilà et al. (2010).

We adapted the densities of the Nazca Plate bodies from Kirchner (1997) as well. Accordingly, the basalt layer density was defined as 2,900 kg/m<sup>3</sup>, and the eclogite layer density was defined as 3,510 kg/m<sup>3</sup>. The rigid upper olivine layer 1 was assigned a density of 3,400 kg/m<sup>3</sup>. Due to the elevated temperatures in the plastic olivine layer 2, a slightly reduced density of 3,390 kg/m<sup>3</sup> was prescribed to this lower layer.

### 2.3.3. Lithospheric Mantle

Seismic tomography allows obtaining information on the velocity distribution of the lithospheric mantle that can then be used to infer its density structure. The resolution of these models is limited by their data coverage and quality and is typically in the order of a few hundred kilometers (e.g., Feng et al., 2007; Schaeffer & Lebedev, 2013). Since our model covers an area that is several times larger than the potential resolution of those tomographic models, we can use them to assess how density variations in the upper lithospheric mantle affect the results of our study. Therefore, we inverted observed *S* wave velocities from the tomographic models *aVs\_2013\_Tecto* (Assumpção et al., 2013), *3D2016\_03Sv* (Debayle et al., 2016), and *SL2013* (Schaeffer & Lebedev, 2013) to densities following a modified version (Meeßen, 2017) of the approach taken by Goes et al. (2000). Details on the conversion are provided in Appendix B.

We tested the effect of four different mineralogical assemblages on the density distribution in the lithospheric mantle (Table 1) and the gravity forward model. The *xenolith* assemblage represents the most recent data on the mineralogy of the mantle that is available in the study area. This assemblage, characterized by high olivine content, represents the average of 56 to 23 Ma old mantle xenolith assemblages from southern Paraguay (Comin-Chiaramonti et al., 1986). Detailed information on the assemblage of each sample and the normalized average are available in the supporting information. *HP\_Tc2* and *HP\_Tc3* are proposed mineralogies for Tectons at a depth of 100 km and 800°C provided by Griffin et al. (2009). These were calculated from xenolith compositions using the thermodynamic database by Holland and Powell (1998). The term “Tecton” refers to a crust that has been formed or modified during the last 1 Ga (Griffin et al., 2009) and is therefore applicable to the South American craton, as it has been subjected to a series of tectonic events since the Precambrian. We chose those specific Tecton assemblages because they vary strongly in diopside, spinel, and garnet content compared to the xenolith assemblage. Besides those assemblages thought to be representative of the lithospheric mantle beneath the foreland of northern Argentina, we additionally tested the *off-cratonic* assemblages by Shapiro and Ritzwoller (2004). These represent a more fertile mantle, and this assemblage serves as an end member with high iron content.

To transfer the shear wave velocity models to the modeling domain, we interpolated the original data onto a regular, three-dimensional grid (voxel) with a lateral resolution of 50 km and a vertical resolution of 15 km, equivalent to a total of 10 layers between 50 and 200 km depth. These velocity grids were then converted to density and temperature for each mineralogical assemblage listed above.

The resulting density distributions for all mantle voxels are shown in Figure D1. The differences in average density for the same mineralogical assemblage, but varying shear wave velocity model, fall within  $\pm 1$  kg/m<sup>3</sup>. Differences between the individual assemblages lie within  $\pm 8$  kg/m<sup>3</sup>.

For the gravity forward model, we prescribed the lithospheric mantle density to the average of the Assumpção et al. (2013) voxel with xenolith assemblage ( $3,340 \text{ kg/m}^3$ ). The full density variations from all mantle voxels and assemblages were tested during the sensitivity analysis (section 4.1).

#### 2.4. Gravity Forward Modeling

During gravity forward modeling, we calculated the gravity response of the initial structural model. Calculation of this model was carried out using IGMAS+ (©Transinsight GmbH). This software calculates the gravity field from a triangulated, interconnected network of polyhedra along multiple vertical 2-D profiles (working sections). Because IGMAS+ requires laterally continuous surfaces for the triangulation of the interfaces, triangulation errors would occur where a layer has zero thickness and the nodes of two interfaces overlap. The modeled thickness of layers was therefore defined as 1 m where the layer is not present. Equivalent to the lateral target resolution of 25 km, the forward model was subdivided into 73 working sections with a distance of 25 km running E-W. Because we modeled the Bouguer anomaly field, we only implemented the bodies for the depth range from 0 to 200 km bsl and defined the IGMAS+ specific bodies *Top* and *reference* to the average density of all implemented bodies. A table with the densities and volumes used for averaging is available in the supporting information.

In the initial forward model, we regarded the crystalline crust as a body of homogeneous density. Since global observations (e.g., Rudnick & Fountain, 1995) as well as recent seismic experiments in northern Argentina (Perarnau et al., 2012) call for a more complex density structure of the crystalline crust, we can expect that the gravity field of the initial model would deviate from the observed gravity field. This deviation, the gravity residual, indicates which areas of the model exhibit mass deficits or mass excess with regard to the actual density distribution in the lithosphere. We used the residual gravity to assess the density configuration of the crust by following an inverse modeling approach, assuming the difference between the gravity response of the model and the observed gravity was mainly produced by variations in the intracrustal structure of the initial model.

#### 2.5. Gravity Inversion

To obtain a differentiated density distribution for the crystalline crust, we assumed that it is composed of two layers with two different average densities. We defined those layers as the upper ( $2,800 \text{ kg/m}^3$ ) and lower crust ( $3,100 \text{ kg/m}^3$ ). To minimize the gravity residual of the forward model, we inverted for the depth of the intracrustal density interface and kept all other interfaces fixed. In doing so, we applied the *harvester* module (Uieda & Barbosa, 2012), which is part of the open-source *fatiando a terra* library (Uieda et al., 2013) for Python 2.7. The harvester is an iterative algorithm that propagates initial density perturbations (seeds) through a prism mesh (regular mesh of rectangular prisms). After each propagation step, the harvester compares the calculated gravity field with the input gravity field and continues to propagate the densities until the difference between the input and the calculated gravity fields reaches a prescribed minimum threshold. The initial seed distribution in our inversion represented a spatially continuous layer of 500 m thickness at the base of the crystalline crust. To reduce the amount of possible solutions for the inversion, we imposed two boundary conditions on the harvester. First, we modified the harvester to grow seeds only in the upward direction instead of growing them in all directions. Without this modification, the solution would be highly nonunique and would result in heterogeneous bodies with density distributions that could hardly be interpreted. Second, the harvester was restricted to grow seeds only within the volume of the crystalline crust.

The resolution of the prism mesh was set to 25 km laterally and 500 m vertically in order to fit the gravity residual of the initial model (Figure 4). Due to the high vertical resolution, the overall trend of the gravity field could be fitted accurately while the coarse lateral resolution prevented the harvester from fitting small wavelengths, for example, in the northwestern part of the modeling area.

### 3. Results

#### 3.1. Starting Structural Model

The individual depth maps of the major density interfaces and thickness maps of the starting structural model are presented in Figure 2. The thickness distribution of the crystalline crust, as obtained from the compiled sediment thickness data and Moho depth, ranges between 70 km along the Andean orogen in the west and 19 km in the northern domain of the modeled area. It is less than 30 km thick along the Transbrasiliano Lineament. The crust east of the Sierras Pampeanas thickens to 42 km and is limited to the west by the

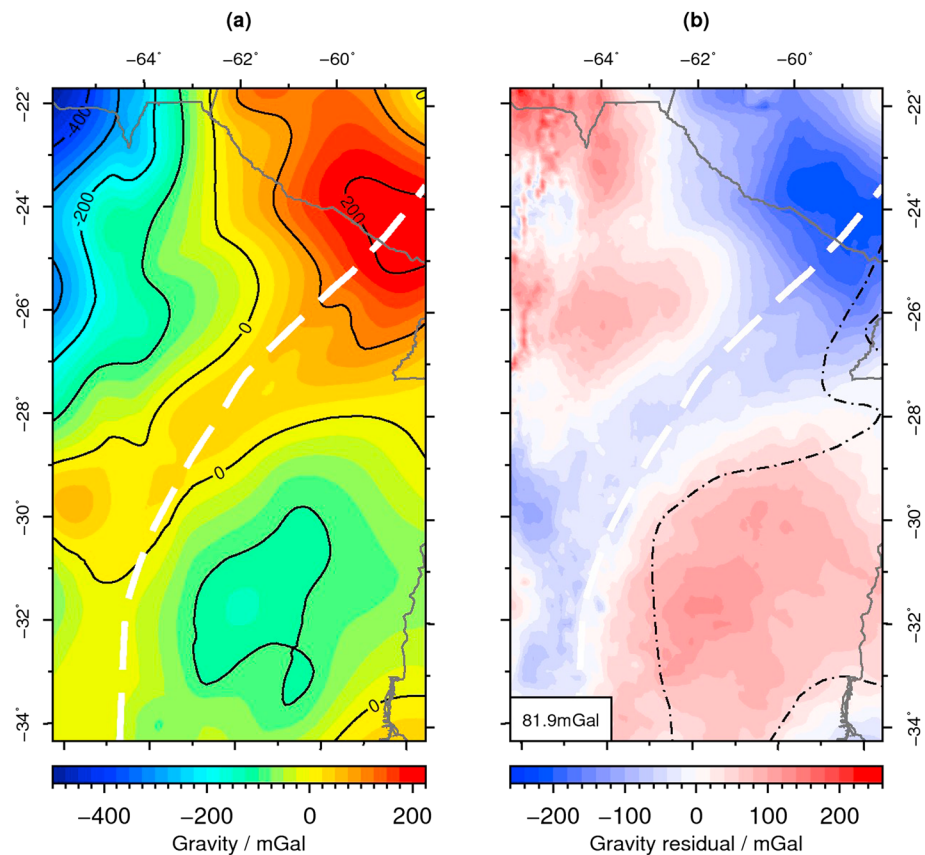


**Figure 4.** Results of forward modeling: (a) calculated Bouguer gravity field, black contours every 100 mGal; (b) residual gravity ( $g_{obs} - g_{calc}$ ). The white dashed line represents the Transbrasiliano Lineament (Peri et al., 2015; Ramos et al., 2010), while the dash-dotted line represents the extent of the Serra Geral flood basalts (Pezzi & Mozetic, 1989). The box in the bottom left corner indicates the root-mean-square (RMS) residual.

boundary between the Pampia terrane and the Río de la Plata craton, which coincide approximately with the Transbrasiliano Lineament in this area.

### 3.2. Gravity Forward Modeling

The calculated gravity field and the gravity residual obtained from the starting model are shown in Figure 4. In the foreland, the observed gravity anomaly (Figure 2d) is characterized by small variations ranging between  $-100$  and  $40$  mGal. To the contrary, the calculated gravity field (Figure 4a) shows strong variations of several  $100$  mGal. The synthetic model resembles the gravity low due to the crustal root of the central Andes in the northwest between  $28$  and  $22^\circ\text{S}$ , but compared to the observed gravity field, it extends too far toward the east. This is apparent in the gravity residual map (Figure 4b) as well. Negative residuals (blue) in Figure 4b indicate mass excess in the model with respect to the observed gravity field, whereas positive residuals (red) indicate mass deficits. As a result, the forward model exhibits mass excess in the southwest and northeast that is connected via a corridor parallel to the Transbrasiliano Lineament. The existence of this corridor is reflected in the morphology of the Moho (Figure 2c) and indicates that the Moho dominates the synthetic gravity field. Positive residuals in the northwest and southeast indicate mass deficits, whereby the southeastern residual, up to  $\approx 120$  mGal, correlates with the extent of Serra Geral flood basalts (dash-dotted line, Figure 4b).

### 3.3. Crustal Structure

The gravity inversion fitted the residual gravity field (Figure 4b) with an RMS fit of  $15.7$  mGal (Figure D2a). Figures 5a and 5b show the distribution of upper and lower crustal thickness as predicted from the inversion procedure. The thickness of the upper crust reaches up to  $39$  km and is greatest in the west beneath the eastern central Andes and the Sierras Pampeanas tectonic province, as well as in the northeast. Upper crust as thin as  $5$  km is predicted beneath the Silurian-Devonian foreland basin in the north and the Neopaleozoic to Mesozoic basin in the central southeast. Most basins (marked 1, 3, and 4 in Figure 2b) are predicted to be

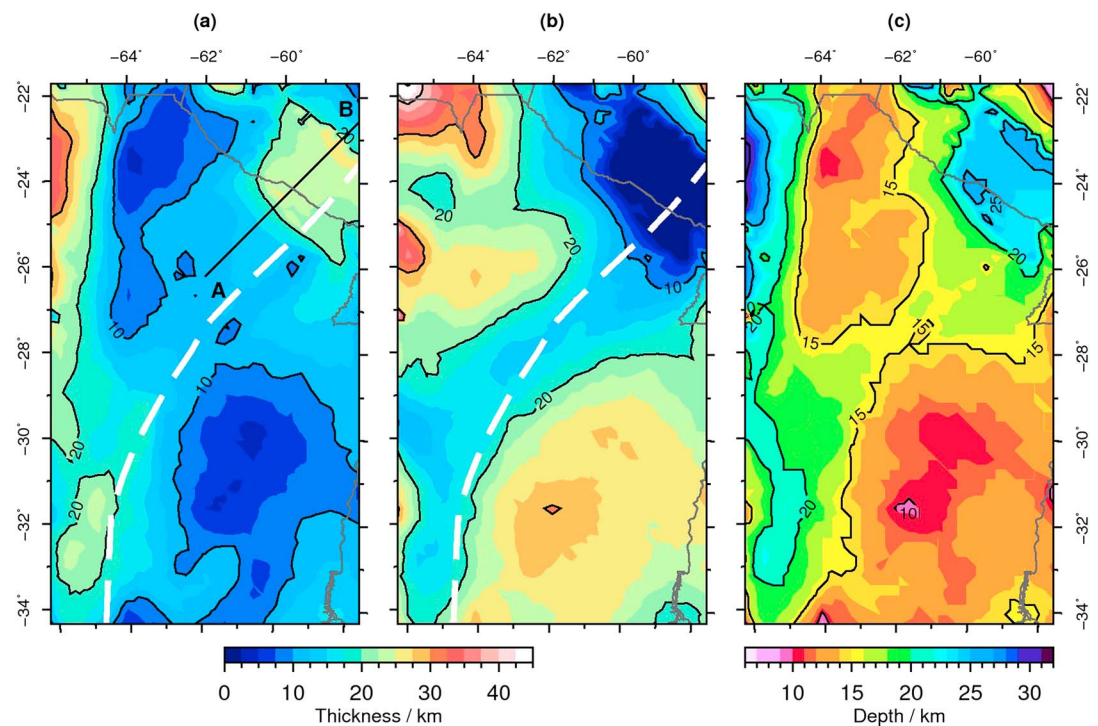


**Figure 5.** Results of gravity inversion. (a) Thickness of the upper crust, (b) thickness of the lower crust, and (c) depth at the top of the lower crust. The dashed line indicates the Transbrasiliano Lineament (Peri et al., 2015; Ramos et al., 2010).

underlain by a lower crust thicker than 15 km, and only the Las Breñas trough is associated with thinner lower crust. Virtually no lower crust is predicted in the northeastern corner of the model. This area coincides with the shallowest parts of the Moho (Figure 2c), which reach depths of 27 to 30 km.

The crustal architecture as derived from gravity inversion can also be treated as a measure of the average density of the crystalline crust (Figure 6a). Analogous to the lower crustal thickness distribution, the average crustal density is low along the Transbrasiliano Lineament. The average crustal density lies at a minimum of  $2,800 \text{ kg/m}^3$  in the northeast and a maximum of  $2,930 \text{ kg/m}^3$  in the northwest.

### 3.4. Isostatic Topography

Assuming local isostasy, we calculated the isostatic topography of the final structural model (for details, see the supporting information). The reference pressure for the calculation at the equilibrium depth of 200 km was defined as the average pressure at the model base of 6.423 GPa. The isostatic topography shown in Figure 6a predicts high relief in the northwest and shallower relief in the Chaco-Paraná plain, parts of which lie below mean sea level. Compared to the actual topography (Figure 6b), the largest differences are observed in the west close to the Andes and the Sierras Pampeanas, where both larger and smaller values are predicted than observed. These differences are elongated in the north-south direction, characterized by a wavelength of 200 to 300 km in the east-west direction, and occur in areas of high topographic elevation.

### 3.5. Mantle Density and Thermal Structure

Sample maps of obtained average mantle density for the xenolith assemblage are shown in Figures 7a–7c. Low densities of approximately  $3,328 \text{ kg/m}^3$  in the north are common between the tomographic models of Assumpção et al. (2013) and Schaeffer and Lebedev (2013). A similarly common feature between both models is a density increase toward the south, although the model of Assumpção et al. (2013) yielded considerably higher densities than the model by Schaeffer and Lebedev (2013). Compared to the first two shear wave models, the magnitude of density variation in the model of Debayle et al. (2016) is considerably lower. Nevertheless, this model indicates a trend of increasing densities as well. Furthermore, the models aVs\_2013\_Tecto and 3D2016\_03Sv both show decreasing densities toward the south.

Overall, the converted temperatures at 100 km depth (Figures 7d–7f) reflect the trends of the average mantle density distributions. High temperatures are predicted from the models by Assumpção et al. (2013)

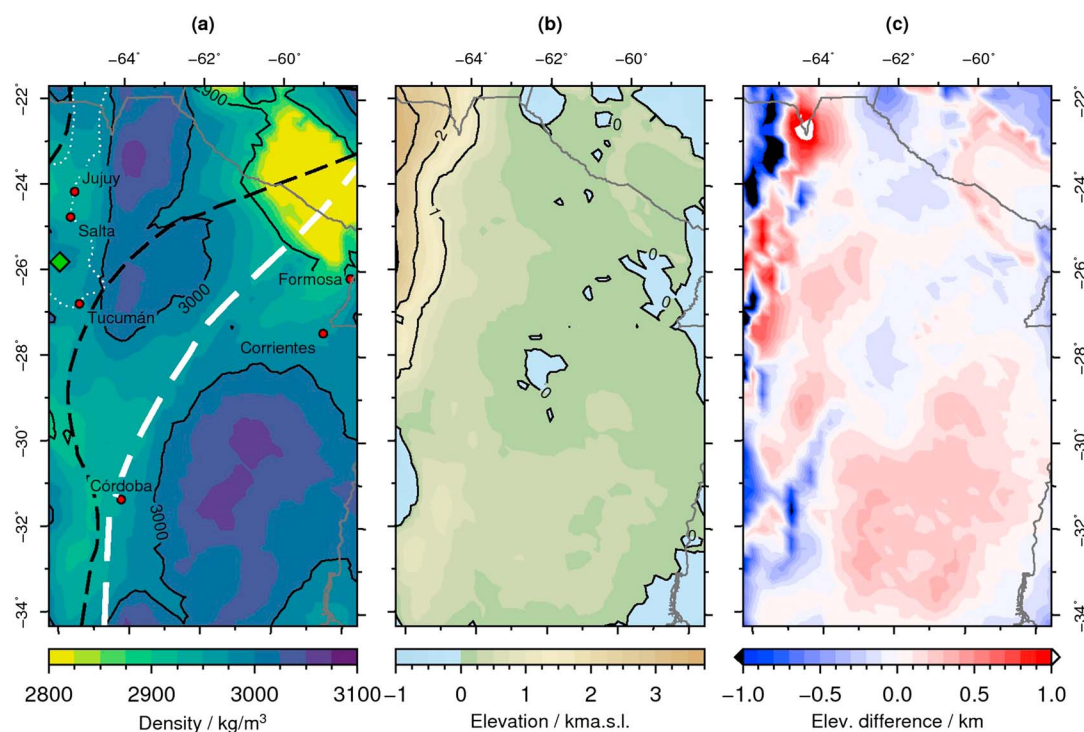


**Figure 6.** Average crustal density and isostatic response of the final model. The black dashed lines represent terrane boundaries by Chernicoff and Zappettini (2004), while the white dashed line represents the Transbrasilian Lineament (Ramos et al., 2010). (a) Average crustal density inferred from the inversion; the green diamond marks the location of lower crustal xenoliths (Lucassen et al., 1999), white dotted line is the present-day extent of the Puncoviscana formation (Escayola et al., 2011). (b) Topographic elevation for an average pressure of 6.423 GPa at the model base. (c) Difference to observed topographic elevation, positive values indicate that our model overestimates the topography.

and Schaeffer and Lebedev (2013), whereas the temperature distribution obtained from Debayle et al. (2016) shows little variation at this depth.

#### 4. Sensitivity Analysis

The input data we used are associated with specific error ranges. Therefore, we tested the sensitivity of our model with respect to variations in sediment density, depth to the top crystalline basement, and mantle density variations.

##### 4.1. Lithospheric Mantle Density

We tested the sensitivity of the model to mantle density variations by imposing densities obtained from shear wave velocity models of the uppermost mantle. We then computed the gravity fields of these models with an inhomogeneous mantle and compared them to the gravity field of the model with a homogeneously dense mantle.

We thus applied the obtained mantle density variations (section 3.5) in the range from depths of 50 to 200 km and then compared the gravity field with the gravity field of the homogeneous model. Those parts of the tomographic model that fall above the Moho depth, that is, sectors within the crystalline crust, were excluded. Where the Moho is shallower than 50 km and a volume of lithospheric mantle is not covered by information from the tomographic model, the density of the lithospheric mantle was set to the average voxel density (Figure D1).

The difference in the forward modeled gravity fields between models with homogeneous mantle and with mantle voxel is shown in Figure 8. The maps show that the shear wave velocity model *aVs\_2013\_Tecto* (Assumpção et al., 2013) has the largest impact on the calculated gravity field, and that the model *3D2016\_Sv* (Debayle et al., 2016) has the least effect. The deviation between the gravity fields of models with homogeneous and inhomogeneous mantle does not exceed  $\pm 55$  mGal.

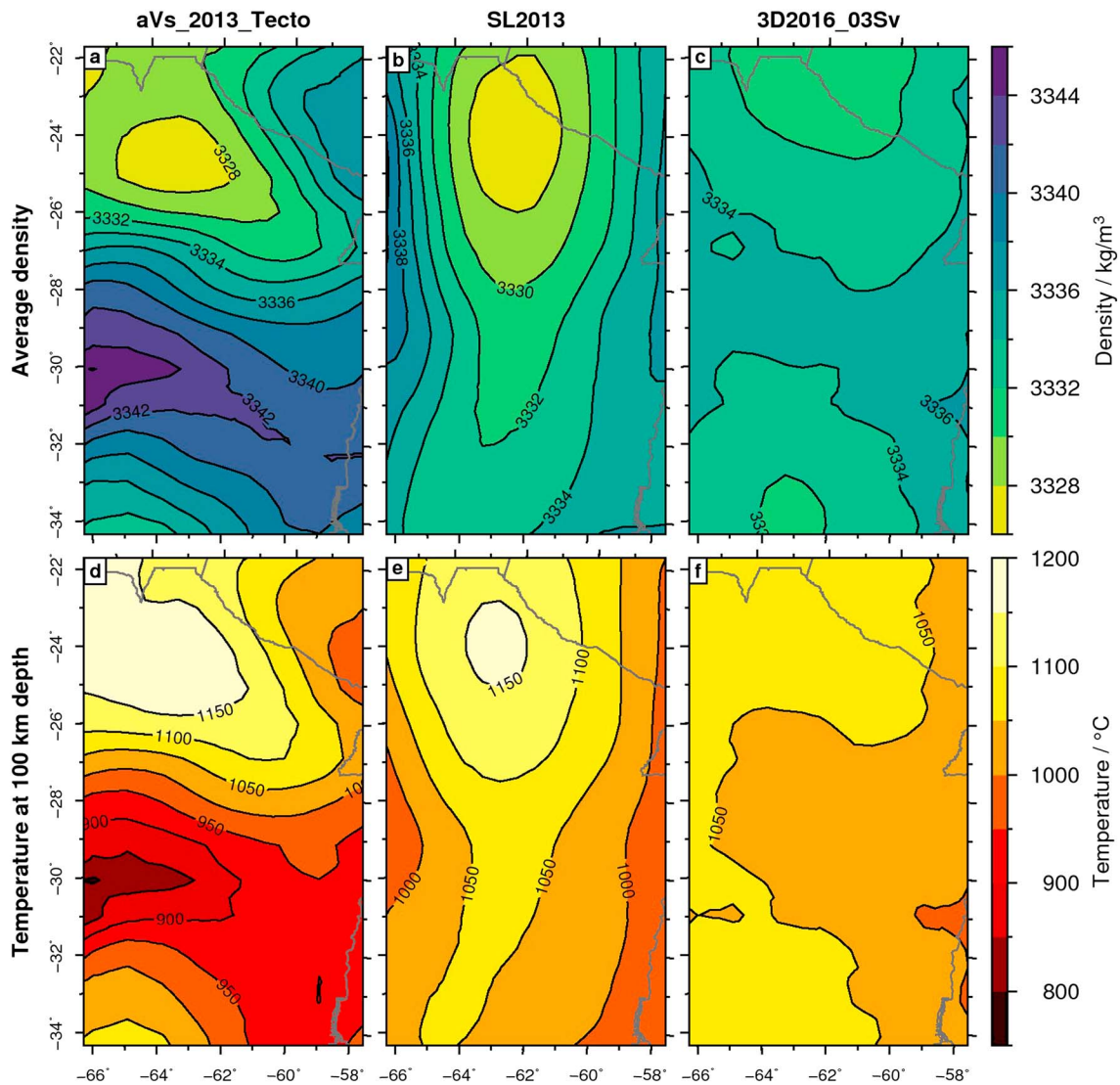


**Figure 7.** Selected results of the density and temperature conversion using the xenolith assemblage (Table 1). (a–c) The average density of the mantle voxels. (d–f) The temperature distribution at approximately 100 km depth. *aVs\_2013\_Tecto* by Assumpção et al. (2013), *SL2013* by Schaeffer and Lebedev (2013), and *3D2016\_03Sv* by Debayle et al. (2016).

To estimate how much these variations influence the resulting lower crustal thickness distribution, we performed an exemplary gravity inversion on *aVs\_2013\_Tecto* applying the xenolith mineral assemblage. The thickness differences of the lower crust between the homogeneous and inhomogeneous mantle models, as inferred from gravity inversion (Figure 9b), largely range around  $\pm 4$  km. In the northwest, the crust in the inhomogeneous mantle model is up to 4 km thicker, while it is up to 4 km thinner in the southern half of the model. The thickened crust compensates for the mass loss that results from less-than-average densities within the lithospheric mantle in the northwestern sector covered by the model. A cross plot of mantle gravity and lower crustal thickness variation reveals an expected good linear correlation with  $R^2 = 0.91$  (Figure 9c), and indicates that for every 10 mGal variation in the gravity field, the inferred lower crustal thickness changes by 1 km.

We used this linear relationship to quantify the impact of the other tomographic models on the inferred thickness distribution of the lower crust. Although the pattern of induced gravity variation between the individual models is significant (Figure 9) for all of the models, the lower crustal thickness would be reduced in the northern part of the model. This reduction, however, would be less than 5 km, which is small compared to the total lower crustal thickness (Figure 5b).

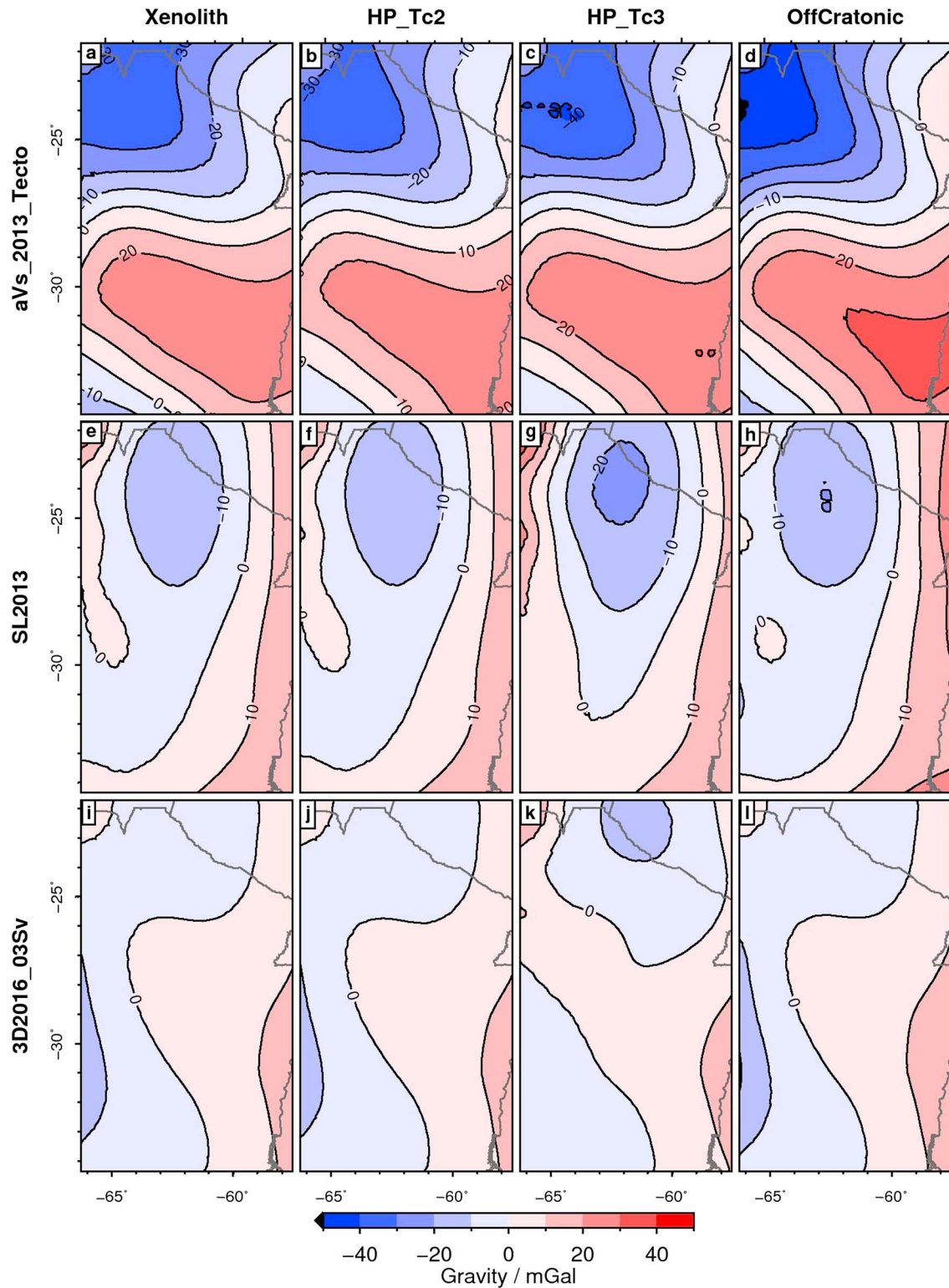


**Figure 8.** Difference maps illustrating the effect of variations in mineralogical assemblages and shear wave velocity models on the forward modeled gravity field. The difference between the forward modeled gravity field  $g_{z,vox}$  of a model and the specified mantle configuration, and the model with a homogeneous mantle  $g_{z,hom}$  (Figure 4a) is shown. The mineral assemblages used are provided in Table 1.

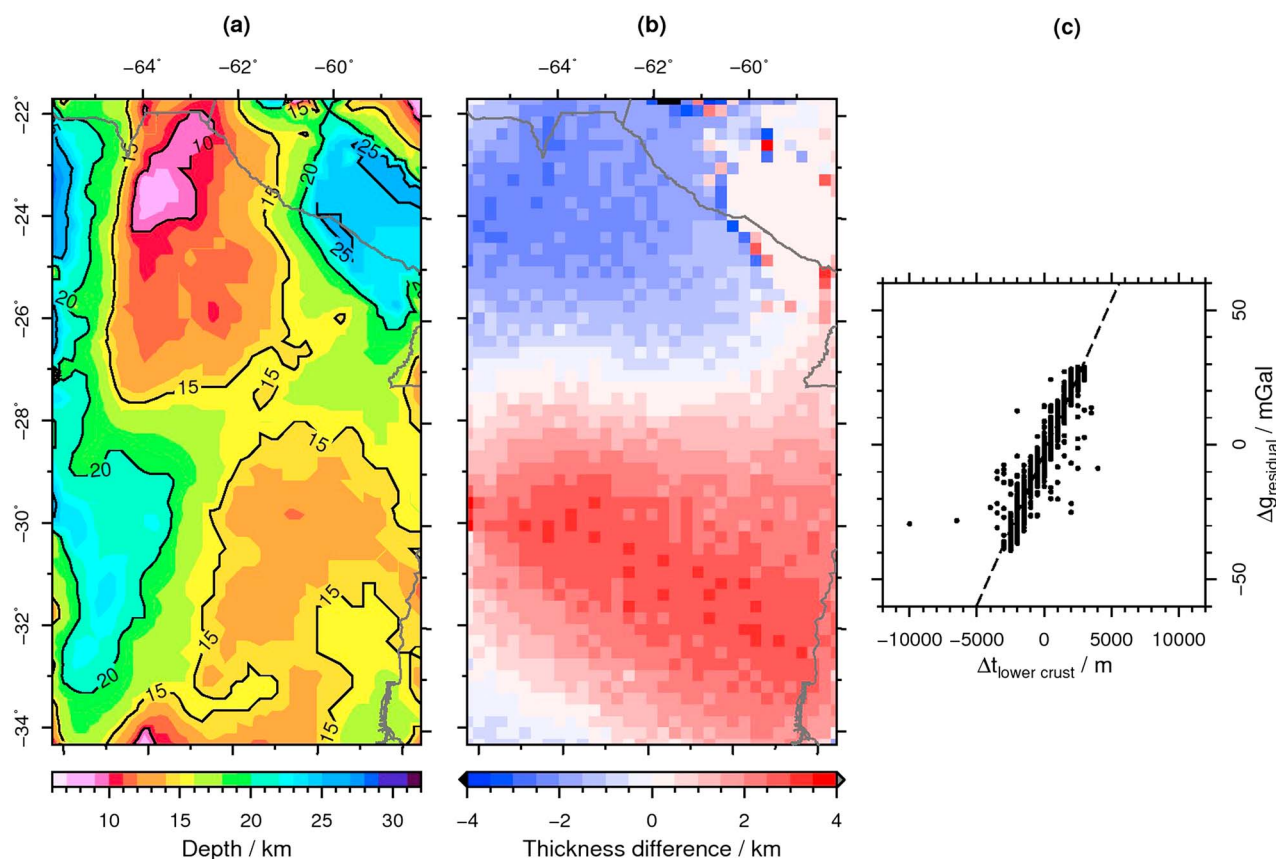


**Figure 9.** Model sensitivity to mantle density variations: (a) Top of the lower crust using the mantle model *aVs\_2013\_Tecto* and xenolith assemblage; (b) lower crustal thickness change in kilometer, positive numbers indicate that the crustal thickness was reduced in the inhomogeneous mantle model with respect to the homogeneous mantle model; (c) cross plot of crustal thickness variations  $\Delta t_{\text{lower crust}}$  versus gravity differences in the reference model  $\Delta g_{\text{residual}}$ . The dashed line represents the best fit with  $\Delta g_z = 0.01 \text{ mGal/m} \cdot \Delta t - 3.13 \text{ mGal}$  and determination coefficient  $R^2 = 0.91$ .

In summary, for every 10 mGal introduced to the gravity field by mantle heterogeneities or other objects the inferred lower crustal thickness changes by about 1 km. Here, we varied the lithospheric mantle density by about  $\pm 30 \text{ kg/m}^3$ , which affects the top of the lower crust by up to  $\pm 4 \text{ km}$  (Table 3).

#### 4.2. Crustal Density

We imposed density variations of  $\pm 50 \text{ kg/m}^3$  on the upper crystalline crust and computed the gravity response of the model. The model with the reduced (increased) density obtained a gravity field up to 20 mGal less (more) in the northeast, and up to 53 mGal more (less) along the central Andes from 28 to 22°S. From the established linear relationship between gravity perturbation and lower crustal thickness variation (section 4.1 and Figure 9c) we reason that the induced thickness variation is in the order of maximum  $\pm 5 \text{ km}$  along the central Andes in the west and up to  $\pm 2 \text{ km}$  in the northeast of the model area. South of 28°S, the possible variation is less than 1 km.

We also tested the sensitivity of the model with respect to variations in the density of the lower crust by varying the density by  $\pm 100 \text{ kg/m}^3$  (equivalent to a 3% variation). The inversion fitted the gravity field well for a  $3,200 \text{ kg/m}^3$  dense lower crust (RMS = 18.4 mGal, Figure D3f). Compared to the thickness of a lower crust at  $3,100 \text{ kg/m}^3$ , the thickness was reduced by about 5 km northwest and southeast of the Transbrasiliano Lineament (Figure D3a) and by about 3 km along the lineament. No variation in thickness was observed in the northeast, where the Moho is shallowest.

In contrast, the inversion was not able to fit the gravity field assuming a  $3,000 \text{ kg/m}^3$  dense lower crust (RMS = 20.5 mGal, Figure D3e), leaving a misfit of about 50 mGal in the area of the Neopaleozoic to Mesozoic depocenters in the southeast (Figure 2b). In the northwest, the lower crustal thickness increased between 4 and 8 km and by about 3 km along the Transbrasiliano Lineament, while it showed no variation in the northeast. The misfit in the southeast is due to the fact that the thickness of the lower crust already reached 100% of

**Table 2**  
Different Lithologies With Compaction Parameter  $k$  and Depositional Porosity  $\phi_0$  (Hantschel & Kauerauf, 2009)

		$k$ ( $\text{km}^{-1}$ )	$\phi_0$	$\rho_s$ ( $\text{kg}/\text{m}^3$ )	$\bar{\rho}$ ( $\text{kg}/\text{m}^3$ )	Difference ( $\text{kg}/\text{m}^3$ )
Sandstone	typical	0.31	0.41	2,720	2,440	0
	clay rich	0.32	0.40	2,760	2,480	40
	clay poor	0.30	0.42	2,700	2,410	-30
	arkose, typical	0.39	0.33	2,730	2,540	100
	quartzite	0.30	0.42	2,640	2,360	-80
Limestone	shaly	0.48	0.50	2,730	2,490	50
Shale	typical	0.83	0.70	2,700	2,500	60

Note. The average density  $\bar{\rho}$  was calculated following equation (A4) for a maximum thickness of 7.2 km. The density difference in the last column states the difference of the average sediment density to typical sandstone, which was used as lithology for the sediment body.

the total crustal thickness in this area, eliminating the possibility to compensate the remaining missing mass. This inability to fit the gravity field indicates that the lower crustal density must be greater than  $3,000 \text{ kg}/\text{m}^3$ .

#### 4.3. Sediment Density

We tested the sensitivity of the model with regard to variations in sediment density by running the inversion twice for a variation of  $\pm 50 \text{ kg}/\text{m}^3$  in the sediment density, which is equivalent to a density variation of 2%. This particular density difference was chosen based on a comparison of the average density of different lithologies that could be expected in the CPB (Table 2).

For a density of  $2,490 \text{ kg}/\text{m}^3$ , the top of the lower crust mostly decreases by 500 to 1,000 m. A decrease of the sediment density to  $2,390 \text{ kg}/\text{m}^3$  leads to a slight increase of the top lower crust by about 500 m. Accordingly, the variation in the topography of the top lower crust is strongest in the northwest and southeast where the deepest depocenters are located.

#### 4.4. Basement Depth

The sediment thickness data were presented by Pezzi and Mozetic (1989) as isopachs for different epochs, as well in the form of a cumulative sediment thickness map. The sum of the individual epoch isopachs and the cumulative thickness information, however, are inconsistent and differ nonsystematically. Additionally, the isopachs were only presented until the end of the Mesozoic units, without information on the thickness distribution of Cenozoic sediments. Data from Marengo (2015) indicate at least 700 m of additional Cenozoic sediments in the area of the Neopaleozoic-Mesozoic depocenter of the CPB (Figure 2b). This additional thickness is a minimum estimate, since the thickness of the Palermo member, which is the earliest Cenozoic member of the Chaco Formation, is missing. We quantified the impact of underestimated sediment thickness on the modeling results by rescaling the sediment thickness distribution (Figure 2e). In areas with a thickness in excess of 1 km an additional 10% was added to the thickness at each point, whereas areas with less than 1 km thick sediments were not edited, as this would have added sediment thickness in areas of outcropping basement. The amount of additional sediment thickness is shown in Figure 10a.

Due to increased sediment thickness, the amount of low-density sediments close to the topography increases while the basement, representing the uppermost density contrast in the subsurface, moves farther down. This overall mass reduction at the surface results in more negative gravity anomalies predicted in the areas of greatest sediment thickness (Figure 10b). In contrast, slightly higher anomalies are predicted in areas of thin sedimentary cover. This increase, that is, the gravity shift, is an effect that is introduced during the calculation of the gravity field. A gravity shift needs to be applied on calculated gravity fields to make it comparable to the measured gravity field. The absolute variation in gravity due to the increased sediment thickness is about 15 mGal.

The difference in the gravity field is in turn reflected by variations in the inverted lower crustal thickness (Figure 10c). The pattern of thickness variation appears noisy, which is attributed to the nonunique inversion algorithm and the fact that lower crustal thickness is added in increments of 500 m. However, areas of reduced gravity also correspond to an overall reduction in lower crustal thickness (Figure 10c). This reduction is not

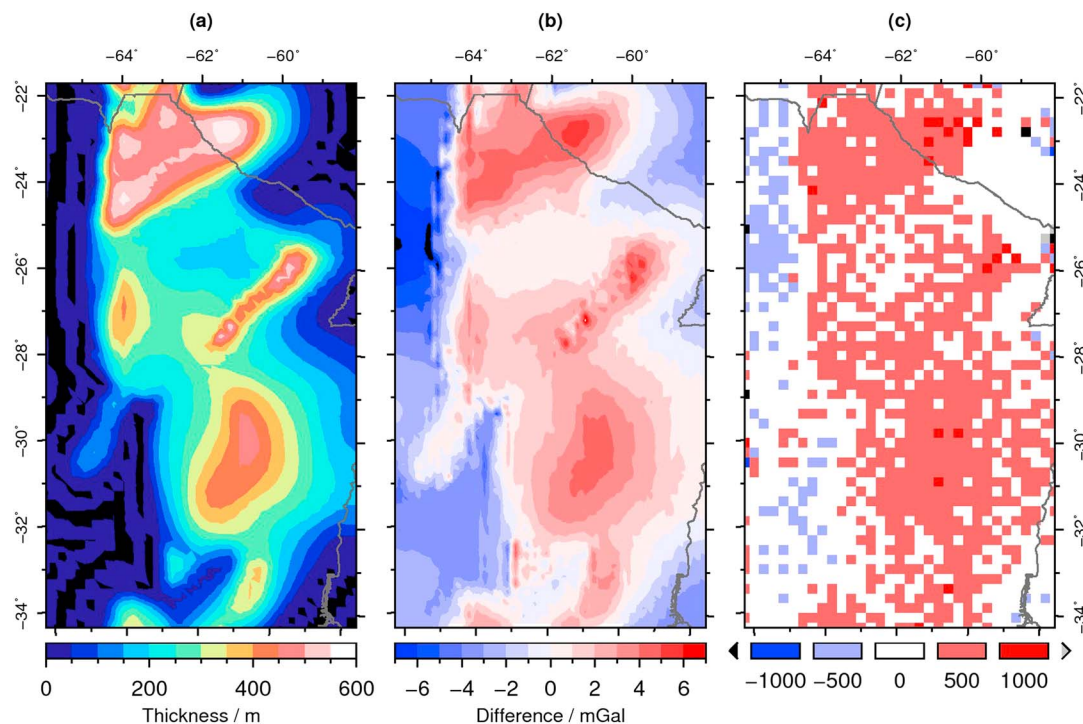


**Figure 10.** Model sensitivity to basement depth variations: (a) sediment thickness difference imposed on the sensitivity model. Sediments in the Neopaleozoic depocenter are about 450 m thicker than in the standard model, (b) the difference between calculated gravity fields. Negative values indicate mass deficit in the sensitivity model with respect to the standard model, (c) the difference in inverted lower crustal thickness. Negative values indicate that the lower crust in the sensitivity model is thicker than in the previous models.

larger than 500 m and is restricted to small areas beneath thin sediment cover. Beneath the areas of increased sediment thickness, we observe an increase of lower crustal thickness by 500 m. Only very locally lower crustal thickness increases by 1,000 m.

We conclude that inaccurate sediment thickness data impact the predicted lower crustal thickness by  $\pm 500$  m. Compared to the absolute thicknesses of several tens of kilometers, this is, however, an acceptable deviation.

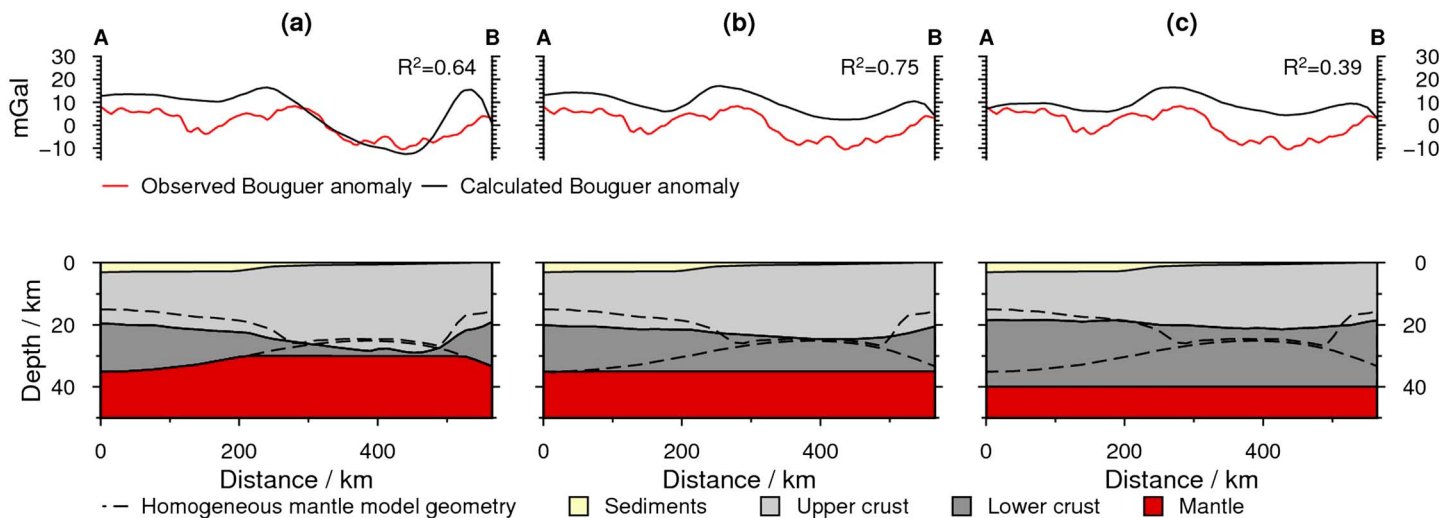


**Figure 11.** Profiles showing test configurations (below) together with the gravity residuals after the inversion (top). Profile location is provided in Figure 5a. (a) Moho capped at 30 km depth. (b) Moho capped at 35 km depth. (c) Moho capped at 40 km depth.  $R^2$  is the determination coefficient between  $g_{z,obs}$  and  $g_{z,calc}$ .

**Table 3**  
Sensitivity Analysis Summary of Various Parameters of the Model on the Induced Variation of the Top of the Lower Crust

Parameter		Imposed variation		Induced variation (km)	$f$ (km/%)
		Rel. (%)	Abs.		
$z$	Basement	10	+0–600 m	$\pm 0.5$	0.05
$\rho$	Sediments	2	$\pm 50 \text{ kg/m}^3$	$\mp 1.0$	0.5
	Upper crust	2	$\pm 50 \text{ kg/m}^3$	$\mp 5$	2.5
	Lower crust	3	$\pm 100 \text{ kg/m}^3$	$\mp 5$	1.7
	Mantle	1	+30 $\text{kg/m}^3$	$\pm 4$	4.0

Note. The factor  $f$  is calculated by dividing the relative variation by the induced variation and is a measure of the extent to which potential errors in the model quantity affect the inferred intracrustal structure.

#### 4.5. Moho Depth

We performed an exemplary analysis on a profile in the northeast of the modeling area to illustrate the sensitivity of the model results to variations in Moho depth. The profile A-B transects an area where the inversion predicts lower crust to be absent and coincides with the shallowest Moho in the modeling area (Figure 2c). As the Moho depth is very shallow and point constraints are far away, this area seems suitable for testing. For the tests, we subsequently limited the Moho depth to depths of 30, 35, and 40 km and then inverted for the top of the lower crust for each depth configuration. The results of the three test models, compared to the homogeneous mantle model, are shown in Figure 11. With decreasing Moho depth, the top of the lower crust above the capped Moho gradually increases from about 28 km for the 30 km deep Moho (Figure 11a) to about 20 km for the 40 km deep Moho (Figure 11c). The calculated gravity fields of the three models is within  $\pm 20$  mGal of the observed Bouguer gravity field, which indicates that they are approximate equally valid solutions for the subsurface. This example demonstrates that, within the given uncertainty of the provided Moho depth, the crustal configuration can change significantly.

#### 4.6. Summary of Sensitivity Analysis

Table 3 provides a summary of the sensitivity analyses conducted. To better compare the impact of the individual model quantities, we calculated a factor  $f$ , which we define as the absolute-induced variation divided by the relative imposed variation.

The factor is a measure of the variation of the top of the lower crust or the lower crustal thickness in response to a change in a model parameter; the variation is expressed as a percentage of each parameter. Using this approach small density variations in the upper lithospheric mantle result in the largest impact on the gravity inversion process in the modeling area. This is owed to the fact that, although the mantle is the deepest body in the model, the mantle volume is the largest component. However, the basement constitutes a major density contrast and, furthermore, is the contrast closest to the gravity stations. Variations in basement depth could be relatively large without altering the main outcomes of this study. Potential variations in Moho depth far away from point constraints exert the largest uncertainty on the model results. However, an increased robustness of the results could only be obtained by more precise depth information on the Moho.

## 5. Discussion

### 5.1. Model Validity

We constrained the density model with geophysical and geological observations and reduced the number of possible solutions by imposing boundary conditions during the inversion. However, a systematic error in our model was introduced by approximating the Earth's surface as in a flat Cartesian coordinate system. With a simplified model (see supporting information), we show that the error due to this simplification is less than  $\pm 5$  mGal. This difference would impose thickness changes of about 500 m to the inferred lower crust but is not significant enough to change the major trends discovered.

We used the calculated isostatic topography (Figure 6b) as a proxy for the robustness of the results. Therefore, we separated the topographic grids into long and short wavelength components using a Gaussian band-pass filter with a wavelength of 500 km. The inferred topographic map reproduces first-order features ( $\lambda \geq 500$  km,

$R^2 = 0.92$ , Figure D4e) such as the central Andes between 28 and 22°S, the Sierras de Córdoba in the southwest, and an extensive flood plain in the remaining model area. There are high-amplitude, short-wavelength deviations (Figure 6c) from the observed topography in the foreland of the orogen that are also reflected in gravity residuals after the inversion (Figure D2a). This deviation is probably an artifact due to local isostasy, where flexural effects play a dominant role, especially in the area of the Andean thrust wedge. On the other hand, in the southern CPB, an area between 34 and 28°S is predicted to have an elevation up to 300 m higher than observed, which indicates that the lithospheric column is too light, resulting in additional uplift. A good fit in the gravity residual (Figure D2a) and the large wavelength of the uplift indicate that mass differences at depth might cause this deviation. In light of the elevated average mantle densities that were obtained from shear wave models (Figures 7a–7c) in the southern part of the model, disregarded masses in the mantle may explain the additional uplift. Optionally, the depth to isostatic equilibrium might be deeper than 200 km in northern Argentina.

Overall, the good agreement of first-order topographic features between observed and predicted topography argues in favor of the model results. We would like to emphasize that the results of this density model are nonunique and that, given other boundary conditions such as a different Moho depth, the outcome may differ from this model. However, in the following we will discuss the results of our model and highlight differences or deviations from geological or geophysical observations that allow robust conclusions.

## 5.2. Structure and Composition of the Crystalline Crust

We use the predicted average density of the crystalline crust (Figure 6a) as an indicator for lateral partitioning. The map is dominated by two high-density provinces ( $> 3,000 \text{ kg/m}^3$ ) in the southeast and northwest, which are surrounded by less dense crust ( $2,900\text{--}2,980 \text{ kg/m}^3$ ). We find that these trends agree well with observations on composition and partitioning of the crust and will discuss the details in the following.

Over the whole model area, the trajectory of the Transbrasiliano Lineament (Ramos et al., 2010) coincides with low-density crystalline crust that originates from a shallow Moho (Figure 2c). Ramos et al. (2010) suggested that the Transbrasiliano Lineament as well as location and trend of the early Paleozoic Las Breñas trough might be related to each other, which together with the shallow Moho might be indicative that the thin crust is a relic of ancient crustal thinning. Since thinning of crust and propagation of rifts along sutures is a well-known process, for example, in the East African Rift (e.g., Hetzel & Strecker, 1994; Smith & Mosley, 1993); therefore, we prefer the location of the Transbrasiliano Lineament by Ramos et al. (2010) over the one proposed by Chernicoff and Zappettini (2004). Accepting the lineament as tectonic boundary, we derive average densities for the Río de la Plata craton of about  $3,000 \text{ kg/m}^3$  and  $2,970 \text{ kg/m}^3$  for the Pampia terrane, excluding the low-density area in the northeast. The Pampia terrane, in addition, seems to be subdivided into a crust with a higher average density to the north ( $3,000 \text{ kg/m}^3$ ) than to the south ( $2,940 \text{ kg/m}^3$ ).

As the greatest part of the Río de la Plata craton in northern Argentina is covered by sedimentary strata of the CPB, its composition is, apart from punctual well data (Rapela et al., 2007; Winn & Steinmetz, 1998), largely unknown. From outcrop and well data in Argentina and Uruguay, Rapela et al. (2007) argued for a rather uniform lithological character of the Río de la Plata craton. Based on the consistently high average crustal density that we obtained east of the Transbrasiliano Lineament (Figure 6a), laterally continuous silica-poor basement rocks throughout the CPB are in agreement with our results.

Observations from outcrops and seismic experiments in the southern Sierras Pampeanas argue for an overall felsic crystalline crust of the Pampia terrane (e.g., Alvarado et al., 2009; Perarnau et al., 2012). At the southern transition between Río de la Plata craton and Pampia terrane (south of 29°S), the average crustal densities in our model decrease from  $> 3,000 \text{ kg/m}^3$  in the east to about  $2,920\text{--}2,960 \text{ kg/m}^3$  beneath the Sierras de Córdoba in the west, arguing for a bulk increase of felsic components. The average density decreases to the west as the top of the lower crust is dipping toward this direction (Figure 5c), resulting in an overall thinner lower crust. This deepening beneath the Sierras de Córdoba agrees with the results by Perarnau et al. (2012), but our model underestimates the depth to the lower crust by about 5 km compared to their results. If we regard the inhomogeneous mantle using the model by Assumpção et al. (2013), the difference in the top to the lower crust (Figure 9a) decreases to about 2–3 km, which is in the range of the error of the receiver functions by Perarnau et al. (2012).

For the northern Pampia terrane lower crustal xenoliths have been used to infer an overall felsic composition of the crystalline crust (Lucassen et al., 1999). Our model agrees with this hypothesis as low densities extend

northward in a narrow band of about 150 km along the thrust wedge of the central Andes. Yet, in a laterally restricted province adjacent to the thrust wedge, the average density of the northern Pampia terrane reaches values comparable to the central Río de la Plata craton, possibly indicating a similar mafic crustal composition. Hacker et al. (2011), on the other hand, demonstrated that not only mafic rocks can attain densities above  $3,000 \text{ kg/m}^3$  at lower crustal levels; rocks of felsic composition such as pelites or wackes can as well if they were previously exposed to extreme P/T conditions ( $1050^\circ\text{C}$  at 3 GPa). Rocks of a similar composition, that is the Puncoviscana formation, were deposited to the west of the crustal high-density province in a peripheral foreland basin at 540 to 524 Ma (Escayola et al., 2011). The authors propose that, during this period, the Puncoviscana formation was deposited on the Arequipa-Antofalla plate, which subsequently subducted beneath the Río de la Plata craton. The sediments of the Puncoviscana could have been exposed to similar P/T conditions during subduction and relaminated to the base of Pampia terrane, a mechanism proposed by Hacker et al. (2011). The present-day extent of the Puncoviscana formation (N of  $27^\circ\text{S}$ ) argues in favor of this hypothesis, as it coincides with the extent of the high-density crust. Based on the sensitivity analyses, we furthermore eliminate inaccurate basement depth, sediment densities, and density variations from the lithospheric mantle as causes for overestimated crustal densities, leaving overestimated Moho depth as an alternative explanation. A bulk change of mineralogy in the crystalline crust could also point to the existence of a still unknown terrane beneath the foreland of the southern central Andes.

Thick lower crust is predicted beneath the CPB in the southeastern sector of the study area (Figure 5b) that spatially coincides with the extent of Serra Geral flood basalts in the CPB (Figure 1). Since the exact depth level of emplacement and the thickness distribution of the basalts are unknown, an error is introduced to the lower crustal thickness estimate. We estimated the maximum impact of the missing basalt layer ( $\rho_{\text{Basalt}} \approx 2,870 \text{ kg/m}^3$ , Christensen & Mooney, 1995) that reaches maximum thickness of  $h_{\text{max}} = 1.2 \text{ km}$  (Chebli et al., 1999) with  $\Delta g \approx 2\pi G h_{\text{max}} (\rho_B - \rho_S)$ , where  $G$  is the gravitational constant and  $\rho_S$  is the sediment density (Figure 3). This estimate yields a maximum impact of the basalt layer of  $\approx 14 \text{ mGal}$  on the gravity field, which is about a magnitude lower than the gravity residual in the forward model (100 to 120 mGal). Since for every 10 mGal, the inferred lower crustal thickness changes by about 1 km (section 4.1), we conclude that the thickness of the lower crust may be overestimated by 1 to 2 km within the extent of the Serra Geral formation. However, this does not significantly change the observation of thick lower crust beneath the southeastern CPB. Similar accumulations of dense lower crust beneath volcanic centers were observed in seismic refraction studies and gravity-constrained models of other areas, such as the Chyulu Hills on the eastern shoulder of the Kenya Rift (Khan et al., 1999; Sippel et al., 2017) or in the Paraná Basin, Brazil (Dragone, 2013). These have been attributed to possible magmatic differentiation and ponding (e.g., Prodehl et al., 1997) of differentiated melts that generated the overlying volcanic provinces. The thickened lower crust may therefore be explained by differentiation processes at the time of Serra Geral volcanism and may be interpreted as magmatic underplating.

### 5.3. Thermal State of the Lithosphere

At depths less than 150 km in particular, the selected tomographic models indicate a trend from low velocities at about  $24^\circ\text{S}$  to higher velocities south of  $28^\circ\text{S}$  (supporting information Figure S10).

At 100 km depth, these velocities translate to temperatures of  $1100\text{--}1200^\circ\text{C}$  in the north, to  $800\text{--}1050^\circ\text{C}$  at about  $30^\circ\text{S}$  (Figures 7d–7f). The wavelength of this variation is greater than the resolution of tomographic models, and as the different models show similar trends, we argue that the foreland lithosphere of the southern central Andes could be warmer than beneath the Sierras Pampeanas. At first glance, this observation contradicts the hypothesis of Babeyko and Sobolev (2005), who proposed a cold and strong lithosphere for the southern central Andes that host the Altiplano, and a warm and weak lithosphere with strong upper crystalline crust for the foreland region that corresponds to the Puna plateau region. However, although the heat input from the lithospheric mantle is important, the heat budget of the crust contributes significantly to the thermal field of the lithosphere, which ultimately affects its strength. Therefore, inferring the rheological state of the lithosphere from tomography-derived temperature maps of the mantle alone would be insufficient.

### 5.4. Implications on the Rheological Behavior of the Lithosphere

From our model results, we derived two principal scenarios for the rheology of the lithosphere in the Andean foreland of northern Argentina. First, if the composition of the high-density crust north of  $28^\circ\text{S}$  is of predominantly felsic composition, the thick crystalline crust might add to the heat budget of the lithosphere and therefore lead to further weakening. Alternatively, if the proportion of mafic crust increases, either due

to magmatic differentiation or compositional change of the entire crystalline crust, the overall heat budget would be reduced due to the low potential of radiogenic heat produced in mafic rocks (Vilà et al., 2010). The latter scenario might support the hypothesis of Babeyko and Sobolev (2005), as such a thick lower crust could compensate for the high heat input from the lithospheric mantle. However, if the first scenario applies, the foreland of the Bolivian Andes should be weak and easily deformable.

Using the presented 3-D model as a basis for assessing the lithospheric-scale thermal field will potentially clarify how temperatures are perturbed by the interaction of the different temperature-controlling factors (i.e., the mantle versus crustal heat contribution). Furthermore, the assessed density configuration of the crust and inferred compositional trends (i.e., mafic versus felsic crust) may be interpreted in terms of rheological trends. Accordingly, the thick lower crust of the Bolivian foreland might be indicative of higher total crustal strengths in this area, given that mafic rocks generally withstand higher deviatoric stresses than felsic rocks before deforming physically (e.g., Carter & Tsenn, 1987). To summarize, our 3-D model indicates thermal and compositional variations along strike the Andean foreland that should be considered when discussing factors responsible for along strike variations in deformation styles.

## 6. Summary and Conclusions

We followed an integrated modeling approach combining forward modeling and inversion to analyze the crustal density structure of the Andean foreland in northern Argentina. The sensitivity of the model was tested in detail with respect to variations in depth and density of individual interfaces and bodies. We find the following.

1. A model with an upper crust of 2,800 kg/m<sup>3</sup> and a lower crust of 3,100 kg/m<sup>3</sup> reproduces the observed gravity field.
2. There is evidence for increasing bulk density of the crystalline crust in the foreland north of 28°S, hinting either a transition to a crust that has a significant proportion of high-density lower crust or a change to a silica-poor bulk composition.
3. Although temperatures converted from shear wave velocities argue in favor of a warm lithospheric mantle beneath the Altiplano foreland and colder mantle beneath the Puna Plateau foreland, an increase of mafic components in the crystalline crust north of 28°S may be indicative of lower amounts of radiogenic heat and thus lower crustal temperatures than in the foreland to the east of the Puna plateau.
4. Thick high-density lower crust spatially correlates with the extent of Jurassic flood basalts and may represent the product of magma differentiation or possible magmatic underplating associated with these massive volcanic extrusions.
5. Extensional processes in the early Paleozoic along the Transbrasiliano Lineament, as proposed by Ramos et al. (2010), might have led to the shallow Moho observed beneath the lineament and the Las Breñas trough.
6. Density variations in the upper lithospheric mantle and the thickness variations in the lower crust have the largest impact on the modeling results for this particular study area.
7. The configuration of the Moho is essential to the density configuration of the crystalline crust, and better data coverage in the CPB would enhance the results of this study.

## Appendix A: Calculation of Average Sediment Density

Athy's law of compaction (Athy, 1930) expresses the density of a fluid-saturated rock as a function of depth  $z$  and porosity  $\phi$ :

$$\rho(z) = \rho_s(1 - \phi(z)) + \phi(z)\rho_L, \quad (A1)$$

where  $\rho_s$  is the solid rock density and  $\rho_L$  is the density of the pore fluid. The porosity  $\phi$  is given by

$$\phi(z) = \phi_0 \cdot e^{-kz}, \quad (A2)$$

with porosity  $\phi_0$  at time of deposition and a lithology-dependent compaction factor  $k$ . The average density  $\bar{\rho}$  of a sediment package with thickness  $t = z - 0$  is then calculated by integrating (A1)

$$\bar{\rho}(z) = \frac{1}{z} \cdot \int_0^z \rho(z) dz, \quad (A3)$$

which yields

$$\bar{\rho}(z) = \rho_s + \frac{\phi_0}{zk} (\rho_L - \rho_s) (1 - e^{-kz}). \quad (A4)$$

**Appendix B: Shear Wave Velocity to Density Conversion**

Goes et al. (2000) calculated the shear wave velocity of a rock with composition  $X$  at pressure  $P$  and temperature  $T$ , including anharmonicity and anelasticity, by

$$v_s(P, T, X, \omega) = \sqrt{\frac{\mu(P, T, X)}{\rho(P, T, X)}} (1 - \xi(\omega, T, a)), \tag{B1}$$

where  $\xi$  describes the attenuation term

$$\xi(\omega, T, a) = \frac{2}{Q(\omega, T) \cdot \tan(\pi a/2)}, \tag{B2}$$

where  $\mu$  is the shear modulus,  $\rho$  is the density, and  $Q$  is the attenuation due to anelasticity depending on the wave frequency  $\omega$  and the frequency exponent  $a$ . For pressures up to about 6 GPa, shear modulus and density can be expressed for each mineral phase in  $X$  with

$$M(P, T) = M_0 + (T - T_0) \frac{\partial M}{\partial T} + (P - P_0) \frac{\partial M}{\partial P} \tag{B3}$$

$$\rho(P, T) = \rho_0 \left( 1 - \alpha_0 (T - T_0) + \frac{P - P_0}{K} \right), \tag{B4}$$

where  $M$  is the bulk modulus  $K$  or shear modulus  $\mu$  and  $\alpha$  is the isobaric expansion coefficient. The mineral properties  $\rho_0$ ,  $M_0$ ,  $\partial M/\partial T$ ,  $\partial M/\partial P$ , and  $\alpha$  for the mantle-rock forming minerals olivine, diopside, and enstatite were adopted from Cammarano et al. (2003), for spinel from Goes et al. (2000), and the attenuation parameters for  $Q$  were obtained from Sobolev et al. (1996).

For all depths in the tomography data set,  $v_s$  was calculated for temperatures between 300 and 3000 K in steps of 1 K and stored in a table along with the density corresponding to each temperature. Depth was converted to pressure using AK135 (Kennett et al., 1995). For a given  $v_s$  at  $z$  of the tomography model, the appropriate density was then obtained by linearly interpolating the densities corresponding to the two closest calculated velocities  $v_s$  in the table. The benefit of the lookup method compared to a numerical solver as used by Goes et al. (2000) is that, for a limited amount of depth values in the data set, it is significantly faster in an interpreter-based programming language like Python.

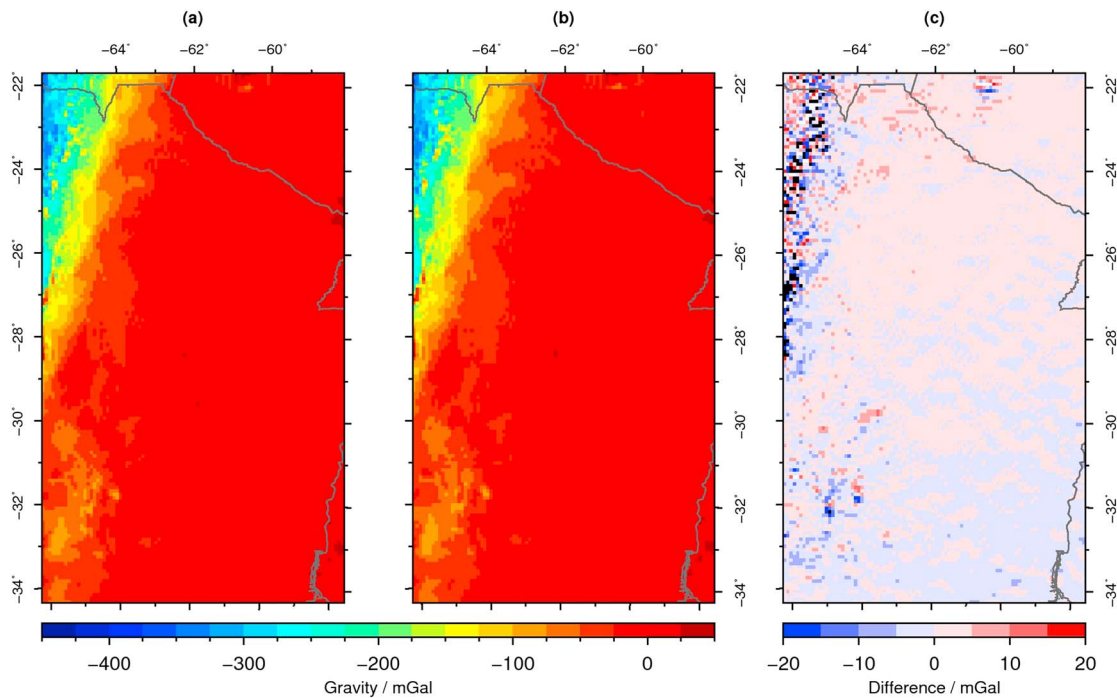


**Figure C1.** Impact of full Bouguer correction: (a) gravity anomaly with simple Bouguer correction using the Bouguer slab (Barthelmes & Köhler, 2012; Förste et al., 2014); (b) gravity anomaly for a full spherical Bouguer correction using *tesseroïds* (Uieda et al., 2016) while considering the Earth’s sphericity and topography; and (c) the difference between the anomaly fields in Figures C1a and C1b.

Appendix C: Bouguer Terrain Correction

As stated in section 2.2.1, we used gravity data that had been reduced to Bouguer using the simple Bouguer slab (Barthelmes & Köhler, 2012; Förste et al., 2014). This correction is efficient in terms of computation as it neither takes into account sphericity of the Earth nor the hills and valleys of the topography. To assess the effects of these simplifications on the results of our study, we have computed a full Bouguer correction including topographic correction using ETOPO1 expanded to degree and order 2190 downloaded from ICGEM (Barthelmes & Köhler, 2012). This topographic model was set up with a lateral resolution of 0.0822°, equivalent to the maximum degree and order of EIGEN-6C4 (Förste et al., 2014), and the corresponding Bouguer anomalies were calculated using *Tesseroids* by Uieda et al. (2016). Figure C1 compares gravity anomaly fields derived from simple and full Bouguer corrections and illustrates that especially in the Andes and Sierras Pampeanas short-wavelength differences exist. These differences, however, are negligibly small compared to the wavelengths of density variations of the crystalline crust, that is, the unknown in the density modeling procedure.

Appendix D: Supporting Figures

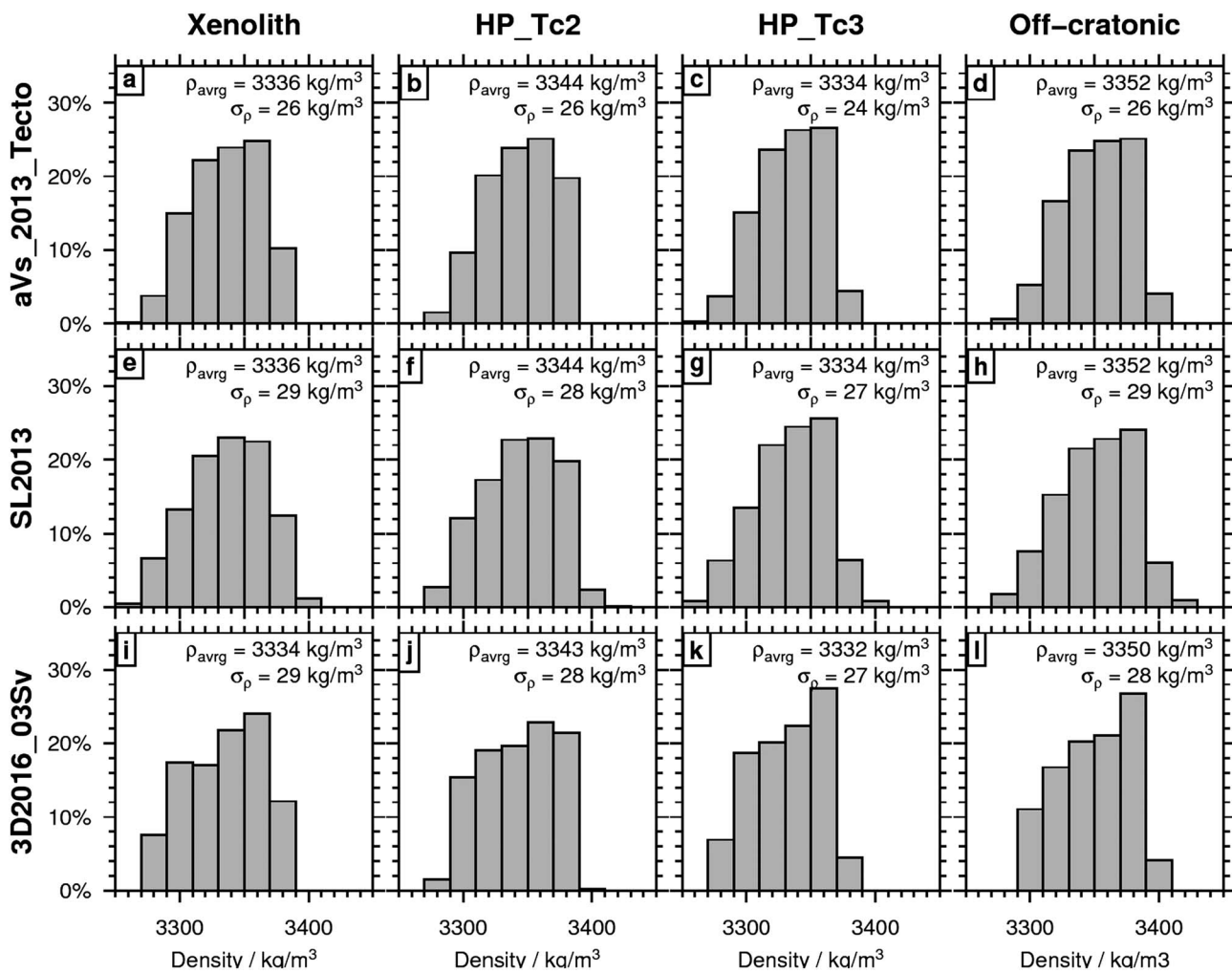
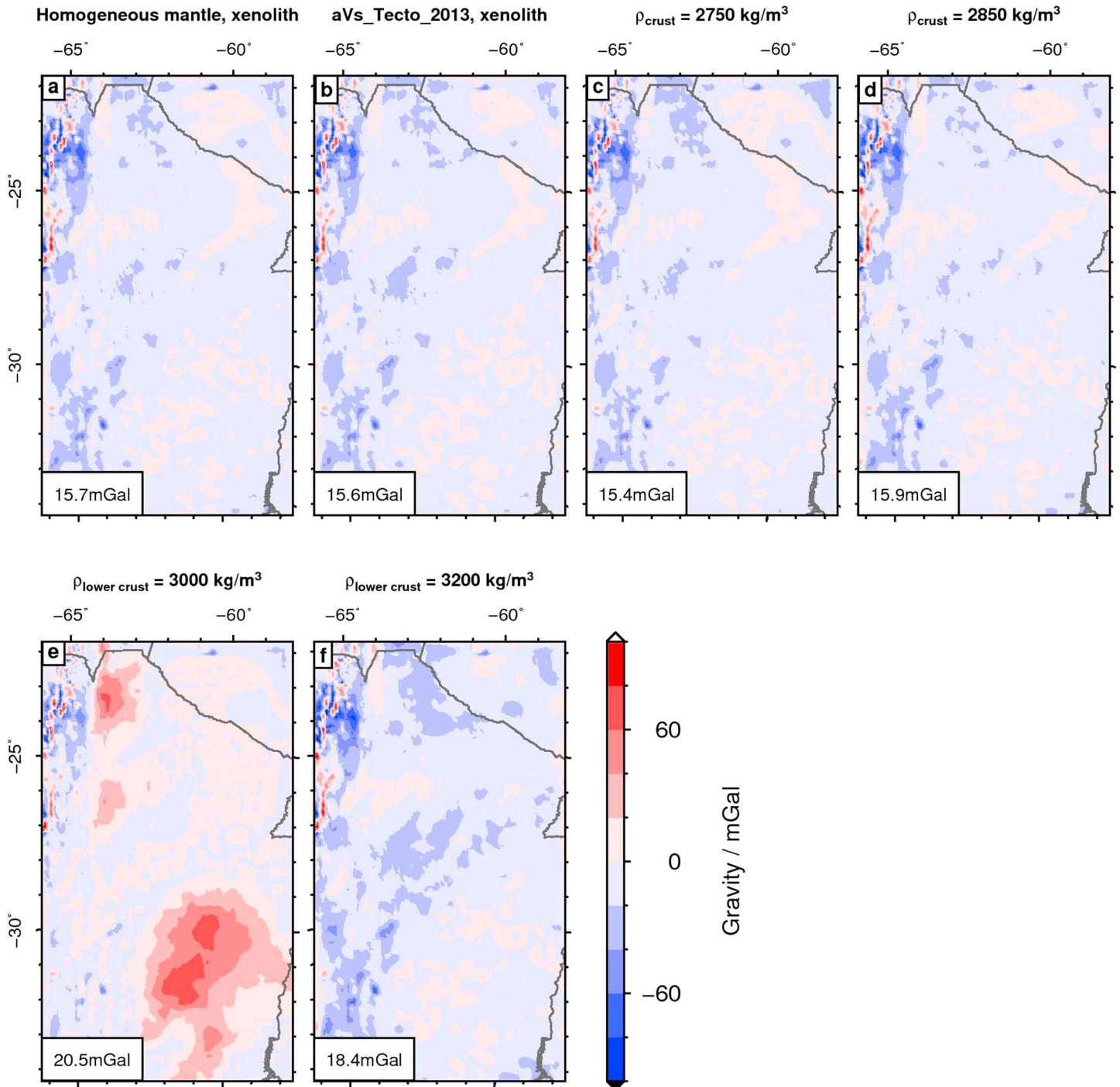
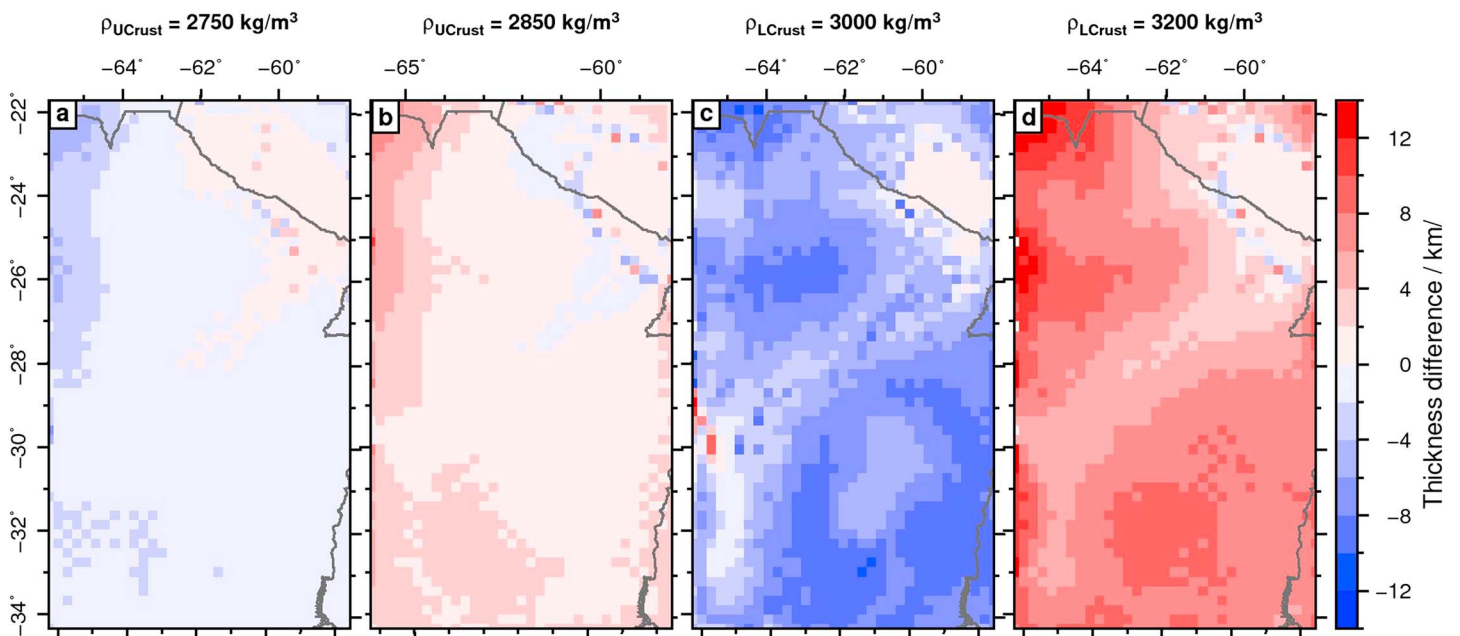


Figure D1. Density histograms of the lithospheric mantle between 50 and 200 km depth for different assemblages obtained from shear wave velocity models. Columns represent assumed mineralogy from Table 1 and rows the used shear wave velocity model (aVs\_2013\_Tecto, Assumpção et al. (2013); SL2013, Schaeffer and Lebedev (2013); and 3D2016\_03Sv, Debayle et al. (2016)). Given also is the average density  $\rho_{avg}$  and the standard deviation  $\sigma_\rho$ . Average density maps are provided in the supporting information, Figure S11.



**Figure D2.** Gravity residuals after inversion. Boxes in the bottom left corners indicate the RMS of the field. (a) Homogeneous mantle with xenolith assemblage, (b) mantle voxel from Assumpção et al. (2013) and xenolith assemblage, (c) sensitivity model upper crust with  $\rho_{\text{UCrust}} = 2,750 \text{ kg/m}^3$ , (d) sensitivity model upper crust with  $\rho_{\text{UCrust}} = 2,850 \text{ kg/m}^3$ , (e) sensitivity model lower crust with  $\rho_{\text{LCrust}} = 3,200 \text{ kg/m}^3$ , and (f) sensitivity model lower crust with  $\rho_{\text{LCrust}} = 3,000 \text{ kg/m}^3$ .



**Figure D3.** Sensitivity of the top of lower crust to density variations in the crystalline crust. For (a) density upper crust of  $2,750 \text{ kg/m}^3$ , (b) density upper crust of  $2,850 \text{ kg/m}^3$ , (c) density lower crust of  $3,000 \text{ kg/m}^3$ , and (d) density lower crust of  $3,200 \text{ kg/m}^3$ .

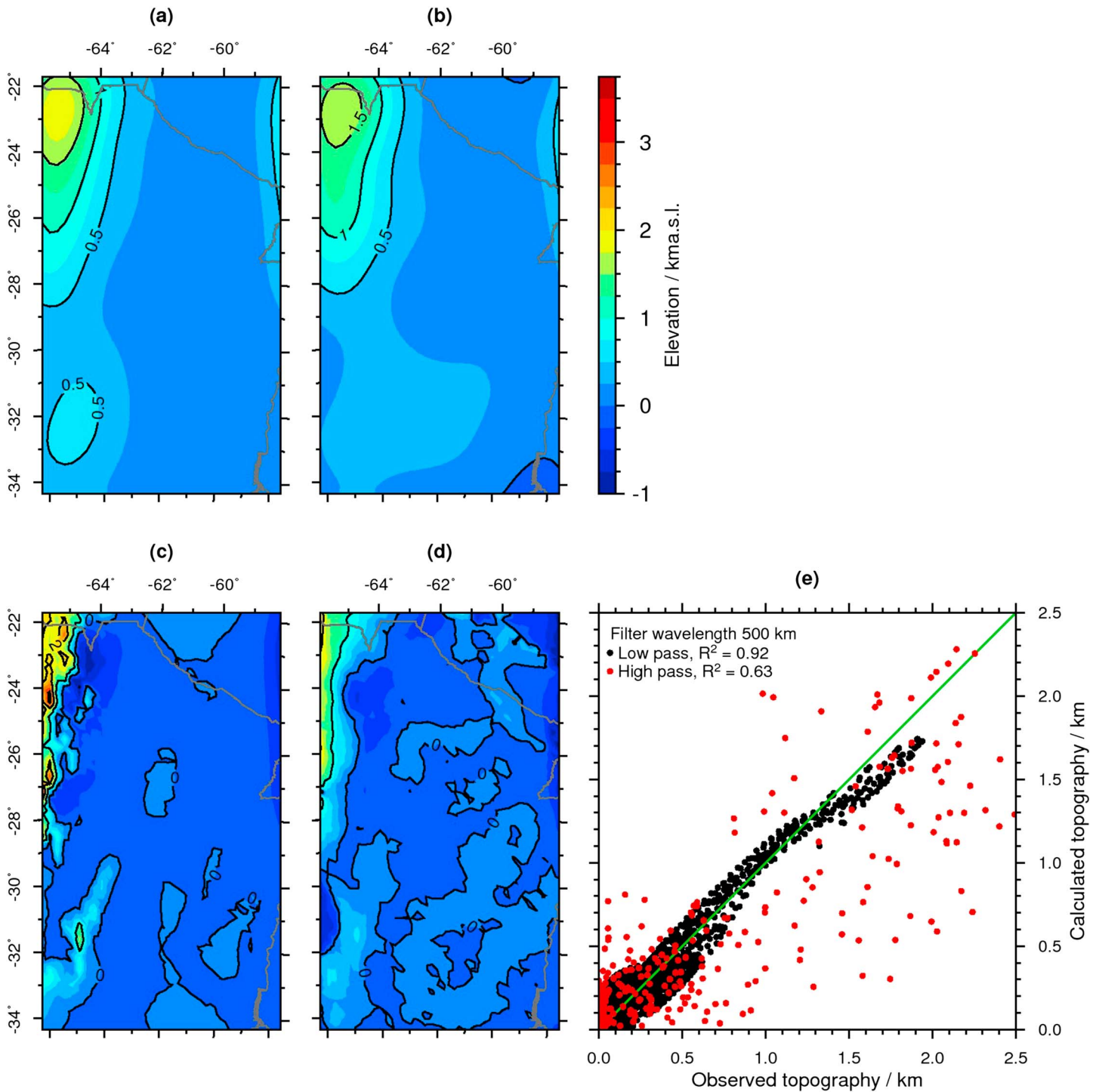


**Figure D4.** FFT-filtered topographic maps. Filtered using a Gaussian bandpass with  $\lambda = 500$  km. (a) Low-pass ETOPO1, (b) low-pass isostatic topography, (c) high-pass ETOPO1, (d) high-pass isostatic topography, and (e) cross plot.

## Acknowledgments

This study was funded by the Deutsche Forschungsgemeinschaft (DFG, grant STR 373/34-1) and the Brandenburg Ministry of Sciences, Research and Cultural Affairs, Germany, within the framework of the international research training group IGK2018 *SuRfAce processes, Tectonics and Georesources: The Andean foreland basin of Argentina* (StRATEGy). We would especially like to thank Mei Feng and Marcelo Assumpção for their great support in providing the shear wave velocities and Moho depths. The topographic color scale used in Figure 2a was adapted from that used by WikiMedia user Lilleskut under the CC BY-SA 3.0 license (<http://creativecommons.org/licenses/by-sa/3.0/deed.en>). All figures were plotted with GMT (Wessel et al., 2013). The data for this model are available as supporting information on the journal website for this article.

## References

- Allmendinger, R. W., Jordan, T. E., Kay, S. M., & Isacks, B. L. (1997). The evolution of the Altiplano-Puna plateau of the central Andes. *Annual Review of Earth and Planetary Sciences*, 25(1), 139–174. <https://doi.org/10.1146/annurev.earth.25.1.139>
- Allmendinger, R. W., Ramos, V. A., Jordan, T. E., Palma, M., & Isacks, B. L. (1983). Paleogeography and Andean structural geometry, northwest Argentina. *Tectonics*, 2(1), 1–16. <https://doi.org/10.1029/TC002i001p00001>
- Allmendinger, R. W., Strecker, M., Eremchuk, J. E., & Francis, P. (1989). Neotectonic deformation of the southern Puna Plateau, northwestern Argentina. *Journal of South American Earth Sciences*, 2(2), 111–130. [https://doi.org/10.1016/0895-9811\(89\)90040-0](https://doi.org/10.1016/0895-9811(89)90040-0)
- Almeida, F. F., Bley de Brito Neves, B., & Dal Ré Carneiro, C. (2000). The origin and evolution of the South American Platform. *Earth Science Reviews*, 50(1–2), 77–111. [https://doi.org/10.1016/S0012-8252\(99\)00072-0](https://doi.org/10.1016/S0012-8252(99)00072-0)
- Alvarado, P., Beck, S., & Zandt, G. (2007). Crustal structure of the south-central Andes Cordillera and backarc region from regional waveform modelling. *Geophysical Journal International*, 170(2), 858–875. <https://doi.org/10.1111/j.1365-246X.2007.03452.x>
- Alvarado, P., Pardo, M., Gilbert, H., Miranda, S., Anderson, M., Saez, M., & Beck, S. (2009). Flat-slab subduction and crustal models for the seismically active Sierras Pampeanas region of Argentina. *Geological Society of America Memoirs*, 204(0), 261–278. [https://doi.org/10.1130/2009.1204\(12\)](https://doi.org/10.1130/2009.1204(12))
- Amante, C., & Eakins, B. W. (2009). *ETOP01 1 arc-minute global relief model*. Procedures: Data Sources and Analysis.
- Assumpcao, M. (1992). The regional intraplate stress field in South America. *Journal of Geophysical Research*, 97(B8), 11,889–11,903. <https://doi.org/10.1029/91JB01590>
- Assumpção, M., Feng, M., Tassara, A., & Julià, J. (2013). Models of crustal thickness for South America from seismic refraction, receiver functions and surface wave tomography. *Tectonophysics*, 609, 82–96. <https://doi.org/10.1016/j.tecto.2012.11.014>
- Athy, L. F. (1930). Density, porosity, and compaction of sedimentary rocks. *AAPG Bulletin*, 14(1), 1–24.
- Babeyko, A. Y., & Sobolev, S. V. (2005). Quantifying different modes of the late Cenozoic shortening in the central Andes. *Geology*, 33(8), 621–624.
- Barthelmes, F., & Köhler, W. (2012). International centre for Global Earth models (ICGEM). *Journal of Geodesy*, 86(10), 932–934.
- Bossi, G. E., Georgieff, S. M., Gavriloff, I. J. C., Ibañez, L. M., & Muruaga, C. M. (2001). Cenozoic evolution of the intramontane Santa María Basin, Pampean Ranges, northwestern Argentina. *Journal of South American Earth Sciences*, 14(7), 725–734. [https://doi.org/10.1016/S0895-9811\(01\)00058-X](https://doi.org/10.1016/S0895-9811(01)00058-X)
- Burov, E., Jaupart, C., & Mareschal, J. C. (1998). Large-scale crustal heterogeneities and lithospheric strength in cratons. *Earth and Planetary Science Letters*, 164(1–2), 205–219. [https://doi.org/10.1016/S0012-821X\(98\)00205-2](https://doi.org/10.1016/S0012-821X(98)00205-2)
- Cahill, T., & Isacks, B. L. (1992). Seismicity and shape of the subducted Nazca Plate. *Journal of Geophysical Research*, 97(B12), 17,503–17,529. <https://doi.org/10.1029/92JB00493>
- Cammarano, F., Goes, S., Vacher, P., & Giardini, D. (2003). Inferring upper-mantle temperatures from seismic velocities. *Physics of the Earth and Planetary Interiors*, 138(3–4), 197–222. [https://doi.org/10.1016/S0031-9201\(03\)00156-0](https://doi.org/10.1016/S0031-9201(03)00156-0)
- Carter, N. L., & Tsenn, M. C. (1987). Flow properties of continental lithosphere. *Tectonophysics*, 136(1–2), 27–63.
- Charrier, R., Ramos, V. A., Tapia, F., & Sagripanti, L. (2015). Tectono-stratigraphic evolution of the Andean orogen between 31 and 37 S (Chile and western Argentina). *Geological Society, London, Special Publications*, 399(1), 13–61. <https://doi.org/10.1144/SP399.20>
- Chebli, G. A., Mozetic, M. E., Rossello, E. A., Bühler, M., & Caminos, R. (1999). Cuencas sedimentarias de la llanura Chacopampeana. In R. Caminos (Ed.), *Anales* (Vol. 29, pp. 627–644). Geología Argentina. Buenos Aires: Instituto de Geología y Recursos Minerales.
- Chernicoff, C. J., & Zappettini, E. O. (2004). Geophysical evidence for terrane boundaries in South-Central Argentina. *Gondwana Research*, 7(4), 1105–1116. [https://doi.org/10.1016/S1342-937X\(05\)71087-X](https://doi.org/10.1016/S1342-937X(05)71087-X)
- Christensen, N. I., & Mooney, W. D. (1995). Seismic velocity structure and composition of the continental crust: A global view. *Journal of Geophysical Research*, 100(B6), 9761–9788. <https://doi.org/10.1029/95JB00259>
- Comin-Chiaromonte, P., Demarchi, G., Girardi, V. A. V., Princivalle, F., & Sinigoi, S. (1986). Evidence of mantle metasomatism and heterogeneity from peridotite inclusions of northeastern Brazil and Paraguay. *Earth and Planetary Science Letters*, 77(2), 203–217. [https://doi.org/10.1016/0012-821X\(86\)90161-5](https://doi.org/10.1016/0012-821X(86)90161-5)
- Cordani, U. G., Pimentel, M. M., Ganade De Araujo, C. E., Basei, M. A. S., Fuck, R. A., & Girardi, V. A. V. (2013). Was there an Ediacaran Clymene Ocean in central South America? *American Journal of Science*, 313(6), 517–539. <https://doi.org/10.2475/06.2013.01>
- Cordani, U. G., & Sato, K. (1999). Crustal evolution of the South American Platform, based on Nd isotopic systematics on granitoid rocks. *Episodes-News magazine of the International Union of Geological Sciences*, 22(3), 167–173.
- Debayle, E., Dubuffet, F., & Durand, S. (2016). An automatically updated S-wave model of the upper mantle and the depth extent of azimuthal anisotropy. *Geophysical Research Letters*, 43, 674–682. <https://doi.org/10.1002/2015GL067329>
- DeCelles, P. G., & Horton, B. K. (2003). Early to middle Tertiary foreland basin development and the history of Andean crustal shortening in Bolivia. *Geological Society of America Bulletin*, 115(1), 58–77. [https://doi.org/10.1130/0016-7606\(2003\)115<0058:ETMTFB>2.0.CO;2](https://doi.org/10.1130/0016-7606(2003)115<0058:ETMTFB>2.0.CO;2)
- Dragone, G. N. (2013). *Estrutura Crustal Da Bacia Do Chaco-Paraná a Partir De Dados Gravimétricos* (Dissertação De Mestrado), Universidade de São Paulo, São Paulo.
- Escayola, M. P., van Staal, C. R., & Davis, W. J. (2011). The age and tectonic setting of the Puncoviscana Formation in northwestern Argentina: An accretionary complex related to Early Cambrian closure of the Puncoviscana Ocean and accretion of the Arequipa-Antofalla block. *Journal of South American Earth Sciences*, 32(4), 438–459. <https://doi.org/10.1016/j.jsames.2011.04.013>
- Exxon (1985). *Tectonic map of the world* (Technical Report). Tulsa, OK, USA: Exxon Production Research.
- Feng, M., van der Lee, S., & Assumpção, M. (2007). Upper mantle structure of South America from joint inversion of waveforms and fundamental mode group velocities of Rayleigh waves. *Journal of Geophysical Research*, 112, B04312. <https://doi.org/10.1029/2006JB004449>
- Fowler, C. M. R. (1990). *The solid Earth: An introduction to global geophysics*. New York: Cambridge University Press.
- Förste, C., Bruinsma, S. L., Abrikosov, O., Lemoine, J. M., Marty, J. C., Flechtner, F., ... Biancale, R. (2014). EIGEN-6c4 The latest combined global gravity field model including GOCE data up to degree and order 2190 of GFZ Potsdam and GRGS Toulouse, GFZ German Research Center for Geosciences. Vienna, Austria: EGU General Assembly, 3707. <https://doi.org/10.5880/icgem.2015.1>
- Goes, S., Govers, R., & Vacher, P. (2000). Shallow mantle temperatures under Europe from P and S wave tomography. *Journal of Geophysical Research*, 105(11), 153–111.
- Griffin, W. L., O'Reilly, S. Y., Afonso, J. C., & Begg, G. C. (2009). The composition and evolution of lithospheric mantle: A re-evaluation and its tectonic implications. *Journal of Petrology*, 50(7), 1185–1204. <https://doi.org/10.1093/ptrology/egn033>
- Hacker, B. R., Kelemen, P. B., & Behn, M. D. (2011). Differentiation of the continental crust by relamination. *Earth and Planetary Science Letters*, 307(3), 501–516. <https://doi.org/10.1016/j.epsl.2011.05.024>
- Hantschel, T., & Kauerauf, A. I. (2009). *Fundamentals of basin and petroleum systems modeling*. Berlin, London: Springer Science and Business Media.

- Heine, C., Yeo, L. G., & Müller, R. D. (2015). Evaluating global paleoshoreline models for the Cretaceous and Cenozoic. *Australian Journal of Earth Sciences*, 62, 275–287. <https://doi.org/10.1080/08120099.2015.1018321>
- Heine, C., Zoethout, J., & Müller, R. D. (2013). Kinematics of the South Atlantic rift. *Solid Earth*, 4(2), 215–253. <https://doi.org/10.5194/se-4-215-2013>
- Hetzl, R., & Strecker, M. R. (1994). Late Mozambique belt structures in western Kenya and their influence on the evolution of the Cenozoic Kenya rift. *Journal of Structural Geology*, 16(2), 189–201. [https://doi.org/10.1016/0191-8141\(94\)90104-X](https://doi.org/10.1016/0191-8141(94)90104-X)
- Holland, T. J. B., & Powell, R. (1998). An internally consistent thermodynamic data set for phases of petrological interest. *Journal of Metamorphic Geology*, 16(3), 309–343. <https://doi.org/10.1111/j.1525-1314.1998.00140.x>
- Isacks, B. L. (1988). Uplift of the central Andean Plateau and bending of the Bolivian procline. *Journal of Geophysical Research*, 93(B4), 3211–3231. <https://doi.org/10.1029/JB093iB04p03211>
- Johnston, A. C., & Schweig, E. S. (1996). The enigma of the New Madrid earthquakes of 1811–1812. *Annual Review of Earth and Planetary Sciences*, 24(1), 339–384. <https://doi.org/10.1146/annurev.earth.24.1.339>
- Jordan, T. E., Isacks, B. L., Allmendinger, R. W., Brewer, J. A., Ramos, V. A., & Ando, C. J. (1983). Andean tectonics related to geometry of subducted Nazca Plate. *Geological Society of America Bulletin*, 94(3), 341–361. [https://doi.org/10.1130/0016-7606\(1983\)94<341:ATRTGO>2.0.CO;2](https://doi.org/10.1130/0016-7606(1983)94<341:ATRTGO>2.0.CO;2)
- Kennett, B. L. N., Engdahl, E. R., & Buland, R. (1995). Constraints on seismic velocities in the Earth from traveltimes. *Geophysical Journal International*, 122(1), 108–124. <https://doi.org/10.1111/j.1365-246X.1995.tb03540.x>
- Khan, M. A., Mechie, J., Birt, C., Byrne, G., Gaciri, S., Jacob, B., ... Thybo, H. (1999). The lithospheric structure of the Kenya rift as revealed by wide-angle seismic measurements. *Geological Society, London, Special Publications*, 164(1), 257–269. <https://doi.org/10.1144/GSL.SP.1999.164.01.13>
- Kirchner, A. (1997). 3d-Dichtemodellierung zur Anpassung des Schwere- und des Schwerepotentialfeldes der zentralen Anden (Dissertation FU Berlin), Berliner geowissenschaftliche Abhandlungen, Berlin, Germany.
- Kley, J., Monaldi, C. R., & Salfity, J. A. (1999). Along-strike segmentation of the Andean foreland: Causes and consequences. *Tectonophysics*, 301(1–2), 75–94. [https://doi.org/10.1016/S0040-1951\(98\)90223-2](https://doi.org/10.1016/S0040-1951(98)90223-2)
- Lucassen, F., Becchio, R., Harmon, R., Kasemann, S., Franz, G., Trumbull, R., ... Dulski, P. (2001). Composition and density model of the continental crust at an active continental margin—The central Andes between 21 and 27 S. *Tectonophysics*, 341(1), 195–223.
- Lucassen, F., Lewerenz, S., Franz, G., Viramonte, J., & Mezger, K. (1999). Metamorphism, isotopic ages and composition of lower crustal granulite xenoliths from the Cretaceous Salta rift, Argentina. *Contributions to Mineralogy and Petrology*, 134(4), 325–341. <https://doi.org/10.1007/s004100050488>
- Marengo, H. (2015). *Neogene micropaleontology and stratigraphy of Argentina: The Chaco-Paranense Basin and the Peninsula de Valdés*. Cham: Springer.
- Marot, M., Monfret, T., Gerbault, M., Nolet, G., Ranalli, G., & Pardo, M. (2014). Flat versus normal subduction zones: A comparison based on 3-D regional traveltime tomography and petrological modelling of central Chile and western Argentina (29°35'S). *Geophysical Journal International*, 199(3), 1633–1654. <https://doi.org/10.1093/gji/ggu355>
- MeeBen, C. (2017). *Velocity conversion*. Potsdam: GFZ Data Services. <https://doi.org/10.5880/GFZ.6.1.2017.001>
- Milani, E. J., & Zalan, P. V. (1999). An outline of the geology and petroleum systems of the Paleozoic interior basins of South America. *Episodes*, 22, 199–205.
- Mon, R. (1979). Esquema estructural del Noroeste Argentino. *Revista de la Asociación Geológica Argentina*, 35, 53–60.
- Mpodozis, C., & Ramos, V. (1990). The Andes of Chile and Argentina, *Geology of the Andes and its relation to hydrocarbon and mineral resources* (pp. 59–90). Houston, Tex: Circum Pacific Council Publications.
- Nürnberg, D., & Müller, R. D. (1991). The tectonic evolution of the South Atlantic from Late Jurassic to present. *Tectonophysics*, 191(1–2), 27–53. [https://doi.org/10.1016/0040-1951\(91\)90231-G](https://doi.org/10.1016/0040-1951(91)90231-G)
- Otamendi, J. E., Vujovich, G. I., de la Rosa, J. D., Tibaldi, A. M., Castro, A., Martino, R. D., & Pinotti, L. P. (2009). Geology and petrology of a deep crustal zone from the Famatinian paleo-arc, Sierras de Valle Fértil and La Huerta, San Juan, Argentina. *Journal of South American Earth Sciences*, 27(4), 258–279. <https://doi.org/10.1016/j.jsames.2008.11.007>
- Padula, E., & Mingramm, A. (1963). The fundamental geological pattern of the Chaco-Parana Basin (Argentina) in relation to its oil possibilities, *World Petroleum Congress* (pp. 293–310). Germany: Frankfurt am Main.
- Perarnau, M., Gilbert, H., Alvarado, P., Martino, R., & Anderson, M. (2012). Crustal structure of the Eastern Sierras Pampeanas of Argentina using high frequency local receiver functions. *Tectonophysics*, 580, 208–217. <https://doi.org/10.1016/j.tecto.2012.09.021>
- Peri, V. G., Barcelona, H., Pomposiello, M. C., & Favetto, A. (2015). Magnetotelluric characterization through the Amargasta-Sumampa Range: The connection between the northern and southern trace of the Río de La Plata Craton–Pampean terrane tectonic boundary. *Journal of South American Earth Sciences*, 59, 1–12. <https://doi.org/10.1016/j.jsames.2015.01.003>
- Peri, V. G., Pomposiello, M. C., Favetto, A., Barcelona, H., & Rossello, E. A. (2013). Magnetotelluric evidence of the tectonic boundary between the Río de La Plata Craton and the Pampean terrane (Chaco-Pampean Plain, Argentina): The extension of the Transbrasiliano Lineament. *Tectonophysics*, 608, 685–699. <https://doi.org/10.1016/j.tecto.2013.08.012>
- Pezzi, E. E., & Mozetic, M. E. (1989). Cuencas sedimentarias de la region Chacoparanense, *Cuencas Sedimentarias Argentinas* (pp. 65–78), Serie Correlación Geológica 6. pSan Miguel de Tucumán: Instituto Superior de Correlación Geológica. Universidad de Tucumán.
- Prezzi, C. B., Götze, H.-J., & Schmidt, S. (2014). Andean foreland evolution and flexure in NW Argentina: Chaco–Paraná Basin. *Tectonophysics*, 628, 228–243. <https://doi.org/10.1016/j.tecto.2014.04.041>
- Prodehl, C., Fuchs, K., & Mechie, J. (1997). Seismic-refraction studies of the Afro-Arabian rift system—A brief review. *Tectonophysics*, 278(1–4), 1–13. [https://doi.org/10.1016/S0040-1951\(97\)00091-7](https://doi.org/10.1016/S0040-1951(97)00091-7)
- Ramos, V. A. (1988). Late Proterozoic-early Paleozoic of South American collisional history. *Episodes*, 11(3), 168–174.
- Ramos, V. A. (1999). Las provincias geológicas del territorio Argentino. In R. Caminos (Ed.), *Geología Argentina* (Vol. no. 29 in Anales, pp. 41–96). Buenos Aires: SEGEMAR.
- Ramos, V. A., & Alonso, R. N. (1995). El Mar Paranense en la provincia de Jujuy. *Revista del Instituto de Geología Y Minería*, 10, 73–80.
- Ramos, V. A., Vujovich, G., Martino, R., & Otamendi, J. (2010). Pampia: A large cratonic block missing in the Rodinia supercontinent. *Journal of Geodynamics*, 50(3–4), 243–255. <https://doi.org/10.1016/j.jog.2010.01.019>
- Rapela, C. W., Pankhurst, R. J., Casquet, C., Fanning, C. M., Baldo, E. G., González-Casado, J. M., ... Dahlquist, J. (2007). The Río de la Plata craton and the assembly of SW Gondwana. *Earth-Science Reviews*, 83(1), 49–82. <https://doi.org/10.1016/j.earscirev.2007.03.004>
- Rosa, M. L., Collaço, B., Assumpção, M., Sabbione, N., & Sánchez, G. (2016). Thin crust beneath the Chaco-Paraná Basin by surface-wave tomography. *Journal of South American Earth Sciences*, 66, 1–14. <https://doi.org/10.1016/j.jsames.2015.11.010>
- Rudnick, R. L., & Fountain, D. M. (1995). Nature and composition of the continental crust: A lower crustal perspective. *Reviews of Geophysics*, 33(3), 267–309. <https://doi.org/10.1029/95RG01302>

- Schaeffer, A. J., & Lebedev, S. (2013). Global shear speed structure of the upper mantle and transition zone. *Geophysical Journal International*, 194(1), 417–449. <https://doi.org/10.1093/gji/ggt095>
- Scheck-Wenderoth, M., Cacace, M., Maystrenko, Y. P., Cherubini, Y., Noack, V., Kaiser, B. O., ... Sippel, J. (2014). Models of heat transport in the Central European Basin System: Effective mechanisms at different scales. *Marine and Petroleum Geology*, 55, 315–331. <https://doi.org/10.1016/j.marpetgeo.2014.03.009>
- Schenk, C. J., Viger, R. J., & Anderson, C. P. (2000). Maps showing geology, oil and gas fields, and geologic provinces of the South America region (Technical Report). Denver, CO: USGS.
- Shapiro, N. M., & Ritzwoller, M. H. (2004). Thermodynamic constraints on seismic inversions. *Geophysical Journal International*, 157(3), 1175–1188. <https://doi.org/10.1111/j.1365-246X.2004.02254.x>
- Simpson, C., Law, R. D., Gromet, L., Miro, R., & Northrup, C. (2003). Paleozoic deformation in the Sierras de Cordoba and Sierra de Las Minas, eastern Sierras Pampeanas, Argentina. *Journal of South American Earth Sciences*, 15(7), 749–764. [https://doi.org/10.1016/S0895-9811\(02\)00130-X](https://doi.org/10.1016/S0895-9811(02)00130-X)
- Sippel, J., MeeBen, C., Cacace, M., Mechie, J., Fishwick, S., Heine, C., ... Strecker, M. R. (2017). The Kenya rift revisited: Insights into lithospheric strength through data-driven 3-D gravity and thermal modelling. *Solid Earth*, 8(1), 45–81. <https://doi.org/10.5194/se-8-45-2017>
- Smith, M., & Mosley, P. (1993). Crustal heterogeneity and basement influence on the development of the Kenya rift, East Africa. *Tectonics*, 12(2), 591–606. <https://doi.org/10.1029/92TC01710>
- Snoko, J. A., & James, D. E. (1997). Lithospheric structure of the Chaco and Paraná Basins of South America from surface-wave inversion. *Journal of Geophysical Research*, 102(B2), 2939–2951. <https://doi.org/10.1029/96JB03180>
- Sobolev, S. V., Zeyen, H., Stoll, G., Werling, F., Altherr, R., & Fuchs, K. (1996). Upper mantle temperatures from teleseismic tomography of French Massif Central including effects of composition, mineral reactions, anharmonicity, anelasticity and partial melt. *Earth and Planetary Science Letters*, 139(1–2), 147–163. [https://doi.org/10.1016/0012-821X\(95\)00238-8](https://doi.org/10.1016/0012-821X(95)00238-8)
- Strecker, M. R., Cervený, P., Bloom, A. L., & Malizia, D. (1989). Late Cenozoic tectonism and landscape development in the foreland of the Andes: Northern Sierras Pampeanas (26°–28°S), Argentina. *Tectonics*, 8(3), 517–534. <https://doi.org/10.1029/TC008i003p00517>
- Tassara, A. (2006). Factors controlling the crustal density structure underneath active continental margins with implications for their evolution: Continental margin crustal density. *Geochemistry, Geophysics, Geosystems*, 7(1), Q01001. <https://doi.org/10.1029/2005GC001040>
- Tassara, A., & Echaurren, A. (2012). Anatomy of the Andean subduction zone: Three-dimensional density model upgraded and compared against global-scale models: Anatomy of the Andean subduction zone. *Geophysical Journal International*, 189(1), 161–168. <https://doi.org/10.1111/j.1365-246X.2012.05397.x>
- Uba, C. E., Heubeck, C., & Hulka, C. (2006). Evolution of the late Cenozoic Chaco foreland basin, Southern Bolivia. *Basin Research*, 18(2), 145–170. <https://doi.org/10.1111/j.1365-2117.2006.00291.x>
- Uieda, L., & Barbosa, V. C. (2012). Robust 3D gravity gradient inversion by planting anomalous densities. *Geophysics*, 77(4), G55–G66. <https://doi.org/10.1190/geo2011-0388.1>
- Uieda, L., Oliveira Jr., V. C., & Barbosa, V. C. (2013). Modeling the Earth with Fatiando a Terra. *Proceedings of the 12th Python in Science Conference (SciPy 2013)* (pp. 96–103).
- Uieda, L., Barbosa, V., & Braitenberg, C. (2016). Tesseroids: Forward-modeling gravitational fields in spherical coordinates. *Geophysics*, 81(5), F41–F48. <https://doi.org/10.1190/geo2015-0204.1>
- Vilà, M., Fernández, M., & Jiménez-Munt, I. (2010). Radiogenic heat production variability of some common lithological groups and its significance to lithospheric thermal modeling. *Tectonophysics*, 490(3–4), 152–164. <https://doi.org/10.1016/j.tecto.2010.05.003>
- Wessel, P., Smith, W. H. F., Scharroo, R., Luis, J., & Wobbe, F. (2013). Generic Mapping Tools: Improved version released. *Eos, Transactions American Geophysical Union*, 94(45), 409–410. <https://doi.org/10.1002/2013EO450001>
- Winn, R. D., & Steinmetz, J. C. (1998). Upper Paleozoic strata of the Chaco-Paraná basin, Argentina, and the great Gondwana glaciation. *Journal of South American Earth Sciences*, 11(2), 153–168. [https://doi.org/10.1016/S0895-9811\(98\)00007-8](https://doi.org/10.1016/S0895-9811(98)00007-8)